# Supporting Information

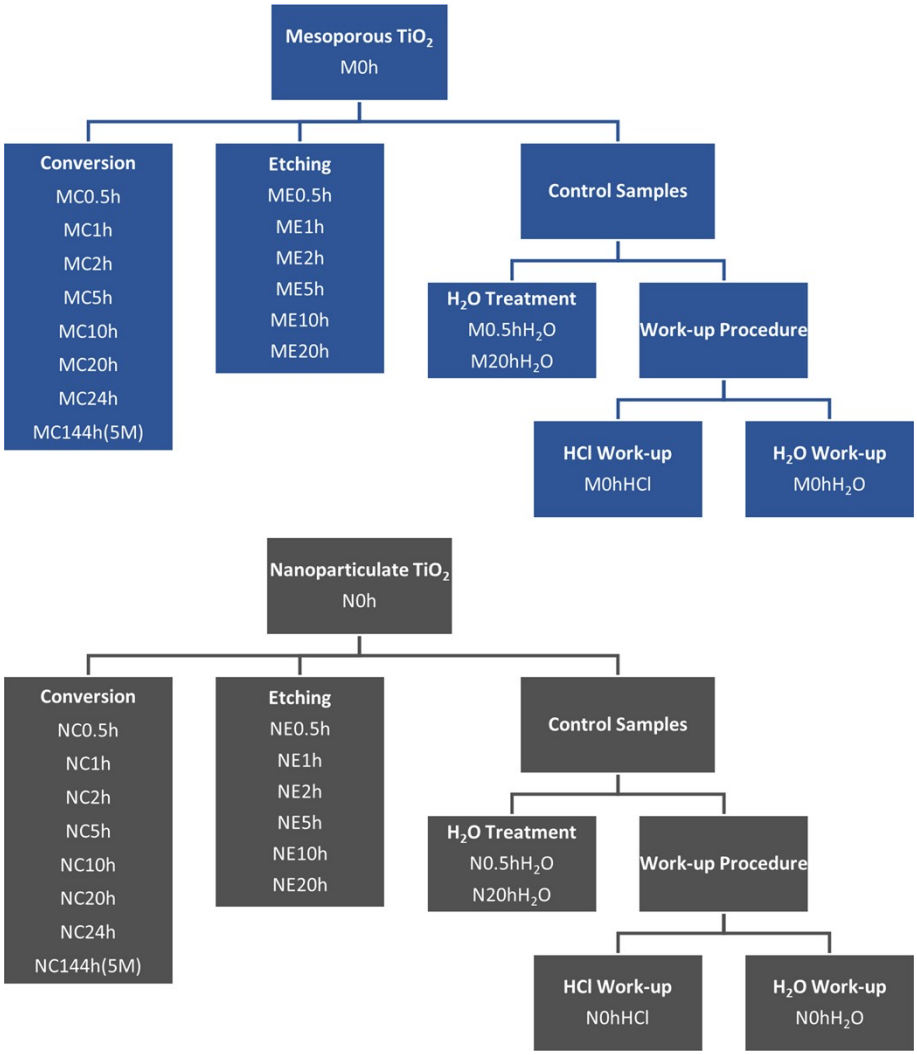


Figure S1: Schematic illustration of the general synthesis concept including designation of the samples.

Table S1: Crystallite sizes (nm) of the MC series.

| phase | M0h | MC0.5h | MC1h | MC2h | MC5h | MC10h | MC20h | MC24h | MC144h(5M) |
|---|---|---|---|---|---|---|---|---|---|
| $TiO_2$ | 20 | 21 | 20 | 21 | 20 | 21 | 21 | 19 | 18 |
| $SrTiO_3$ | - | - | - | 15 | 21 | 21 | 22 | 20 | 21 |

Table S2: Crystallite sizes (nm) of the NC series.

| phase | N0h | NC0.5h | NC1h | NC2h | NC5h | NC10h | NC20h | NC24h | NC144h(5M) |
|---|---|---|---|---|---|---|---|---|---|
| $TiO_2$ | 18 | 18 | 19 | 18 | 19 | 18 | 19 | 19 | - |
| $SrTiO_3$ | - | - | - | 19 | 30 | 28 | 33 | 29 | 34 |

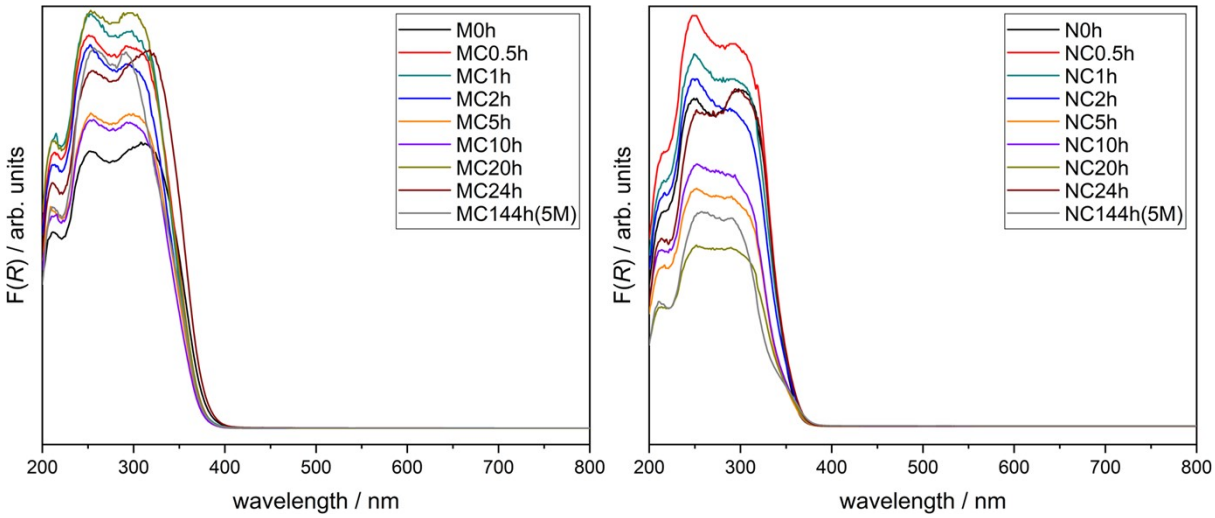


Figure S2: Kubelka-Munk plots of the MC and NC series.

Table S3: Averaged EDX results (at%) of selected samples.

| sample | Sr | Ti | O | C | N | Na | Cl |
|---|---|---|---|---|---|---|---|
| MC1h | 0.1 | 25.6 | 56.5 | 12.0 | 5.7 | 0.0 | 0.1 |
| MC5h | 3.7 | 26.3 | 58.2 | 7.2 | 4.5 | 0.0 | 0.1 |
| MC20h | 3.2 | 24.1 | 55.7 | 14.0 | 2.9 | 0.0 | 0.1 |
| MC144h(5M) | 5.3 | 21.8 | 60.9 | 6.2 | 4.6 | 1.1 | 0.0 |
| NC144h(5M) | 12.4 | 14.3 | 50.1 | 15.2 | 2.0 | 0.7 | 0.0 |

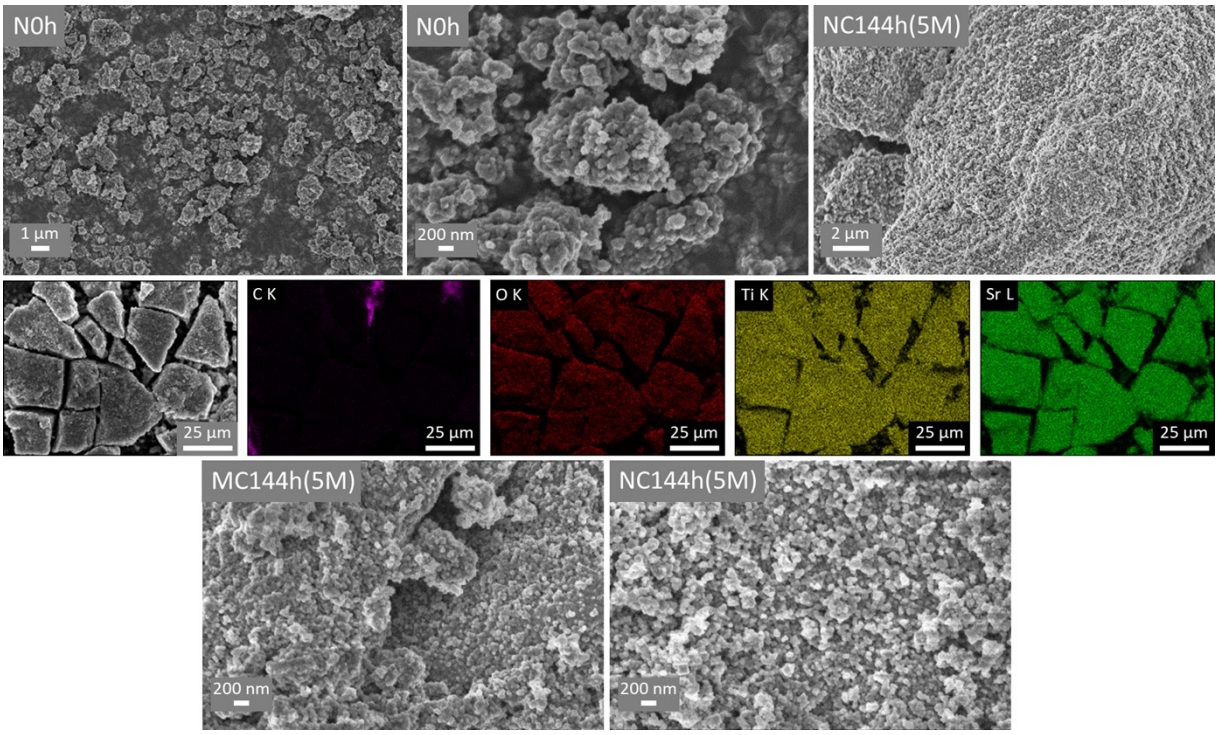


Figure S3: SEM images of the nanoparticulate $TiO_2$ starting material (N0h) and the converted sample NC144h(5M) (top). EDX mapping of NC144h(5M) is shown in the middle and a comparison of $SrTiO_3$ structures of MC144h(5M) and NC144h(5M) is depicted on the bottom.

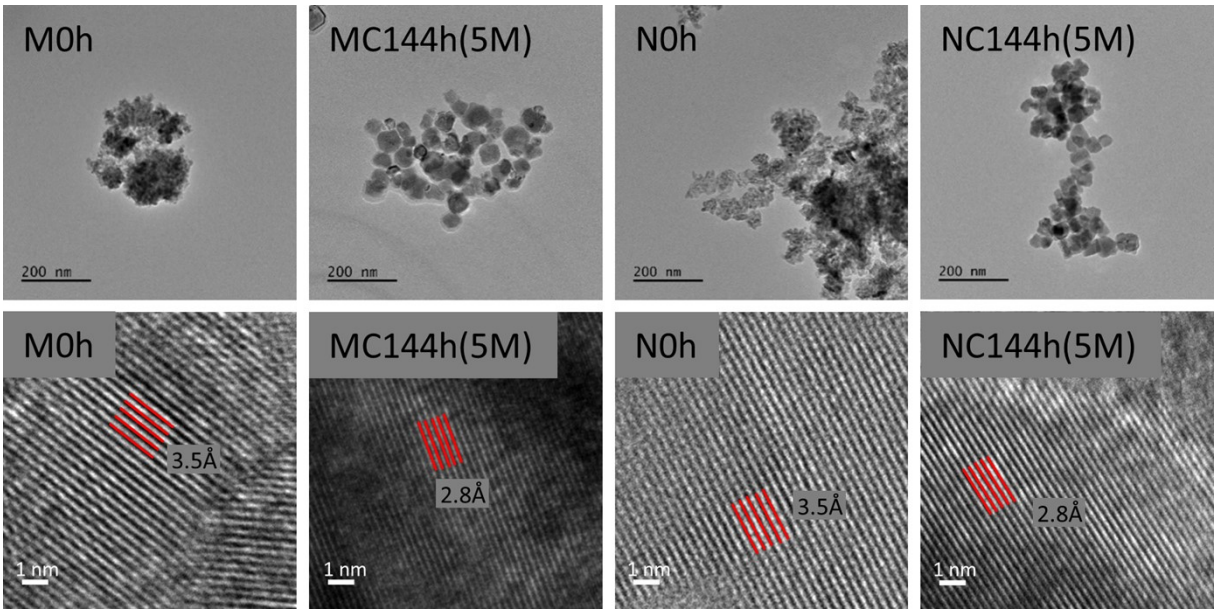


Figure S4: TEM images of the samples M0h, MC144h(5M), N0h, and NC144h(5M).

Table S4: Atomic percentages (at%) of the MC series obtained from XP survey spectra.

| sample | C 1*s* | Sr 3*d* | Ti 2*p* | O 1*s* | Na 1*s* | Cl 2*p* |
|---|---|---|---|---|---|---|
| M0h | 8.34 | - | 26.34 | 65.32 | - | - |
| MC0.5h | 14.66 | 0.23 | 25.42 | 59.09 | - | 0.60 |
| MC1h | 15.48 | 0.58 | 24.22 | 58.77 | - | 0.95 |
| MC2h | 23.76 | 8.42 | 17.58 | 50.25 | - | - |
| MC5h | 14.59 | 17.62 | 15.05 | 52.29 | - | 0.44 |
| MC10h | 14.73 | 17.59 | 15.31 | 51.41 | - | 0.96 |
| MC20h | 13.77 | 17.59 | 14.77 | 53.86 | - | - |
| MC24h | 14.95 | 15.86 | 14.34 | 52.53 | - | 2.33 |
| MC144h(5M) | 11.49 | 17.72 | 14.41 | 54.75 | 1.64 | - |

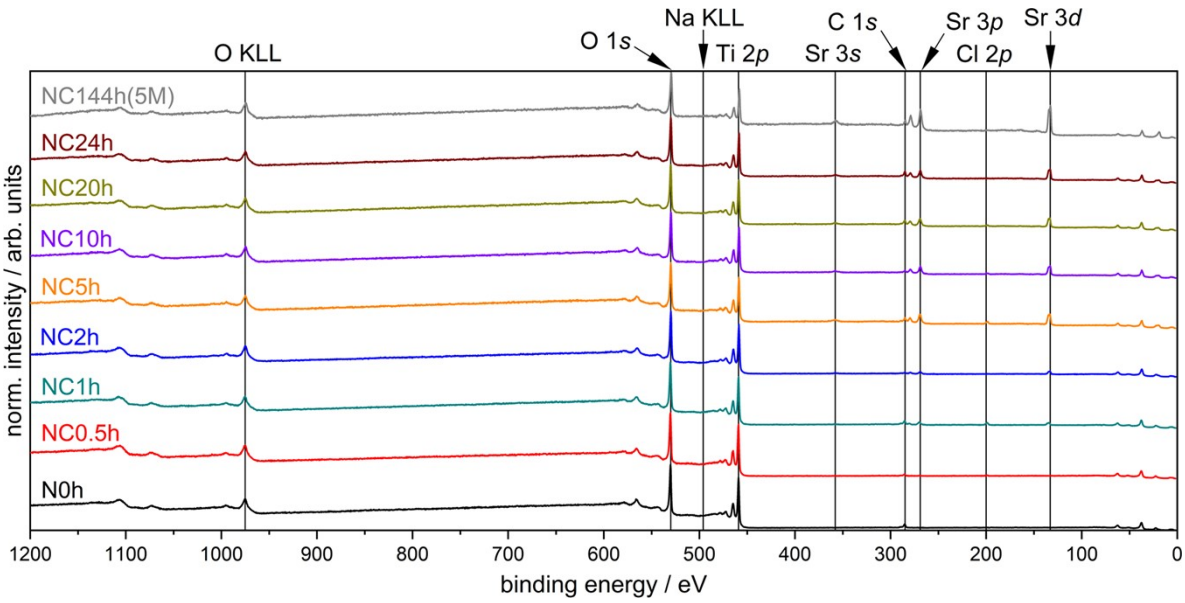


Figure S5: XP survey spectra of the NC series.

Table S5: Atomic percentages (at%) of the NC series obtained from XP survey spectra.

| sample | C 1*s* | Sr 3*d* | Ti 2*p* | O 1*s* | Na 1*s* | Cl 2*p* |
|---|---|---|---|---|---|---|
| N0h | 12.94 | - | 24.43 | 62.64 | - | - |
| NC0.5h | 7.44 | - | 27.92 | 63.73 | - | 0.91 |
| NC1h | 12.25 | 1.47 | 24.44 | 59.62 | - | 2.22 |
| NC2h | 4.30 | 2.27 | 29.27 | 63.99 | - | 0.18 |
| NC5h | 11.4 | 6.98 | 22.49 | 57.00 | - | 2.13 |
| NC10h | 4.10 | 7.30 | 22.85 | 64.75 | - | 1.01 |
| NC20h | 12.07 | 6.46 | 22.06 | 58.03 | - | 1.37 |
| NC24h | 16.00 | 8.15 | 20.71 | 55.13 | - | - |
| NC144h(5M) | 9.30 | 17.67 | 16.54 | 56.49 | - | - |

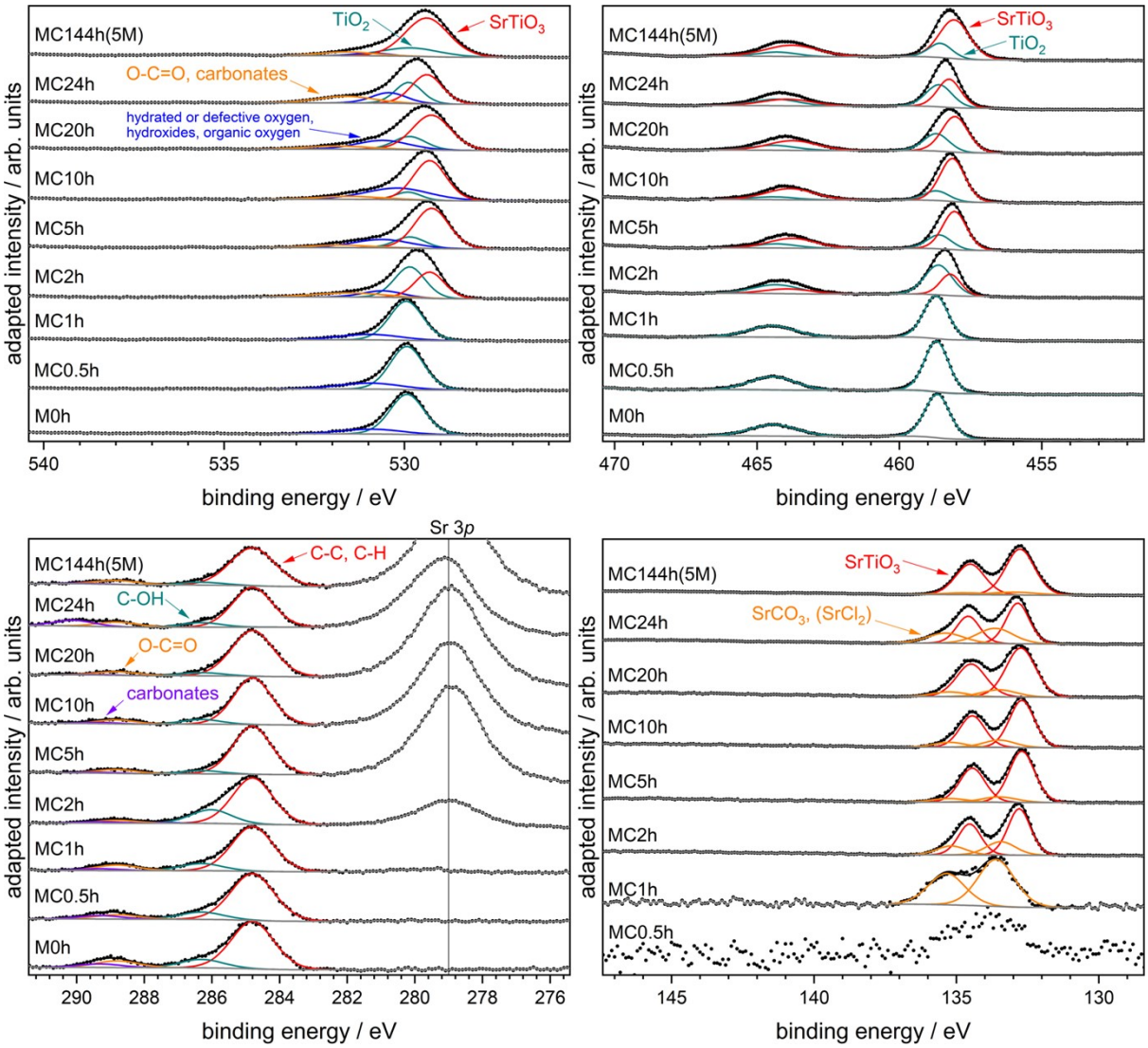


Figure S6: High-resolution XP spectra of the MC series (top left: O 1*s*; top right: Ti 2*p*; bottom left: C 1*s*; bottom right: Sr 3*d*).

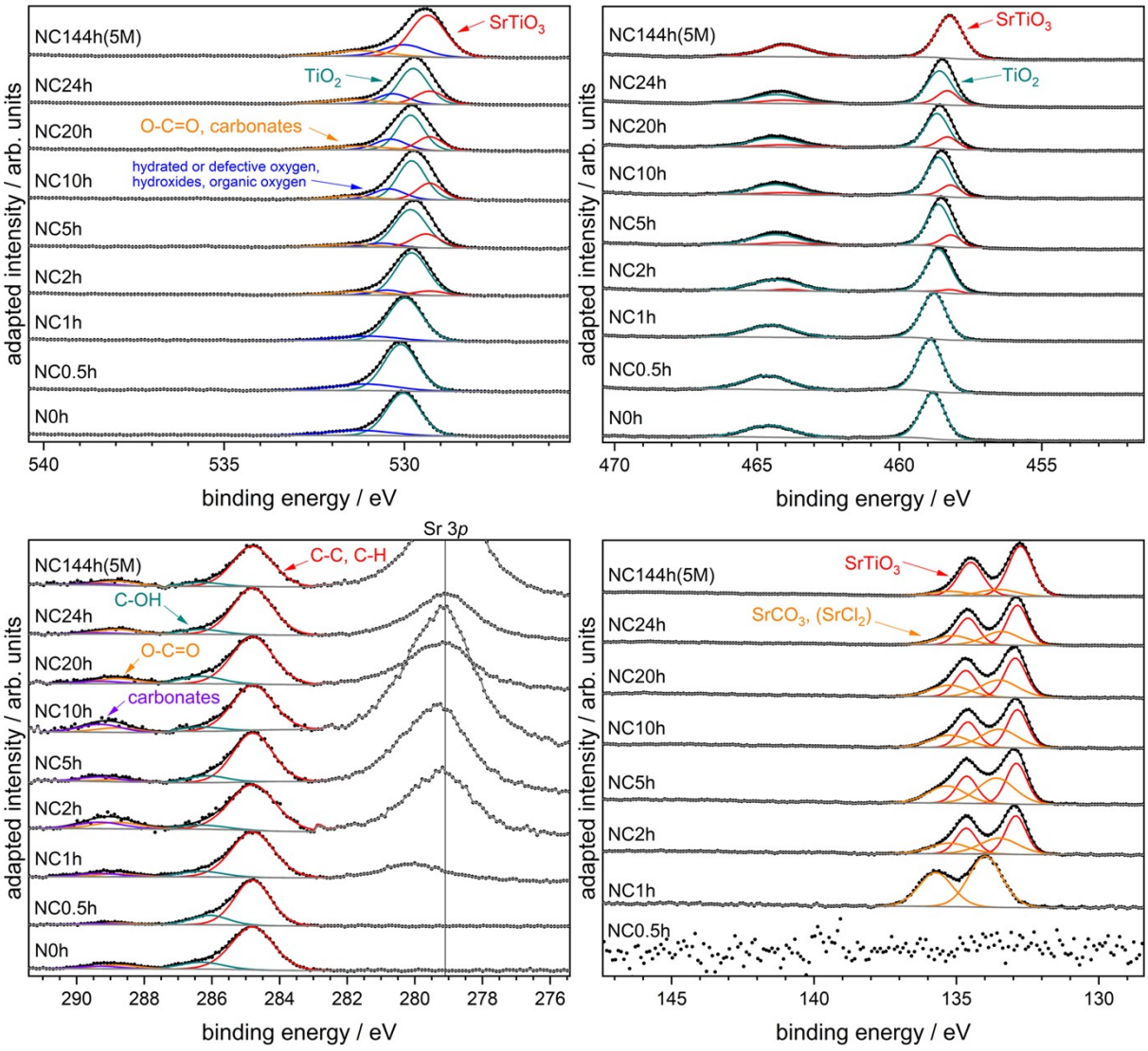


Figure S7: High-resolution XP spectra of the NC series (top left: O 1*s*; top right: Ti 2*p*; bottom left: C 1*s*; bottom right: Sr 3*d*).

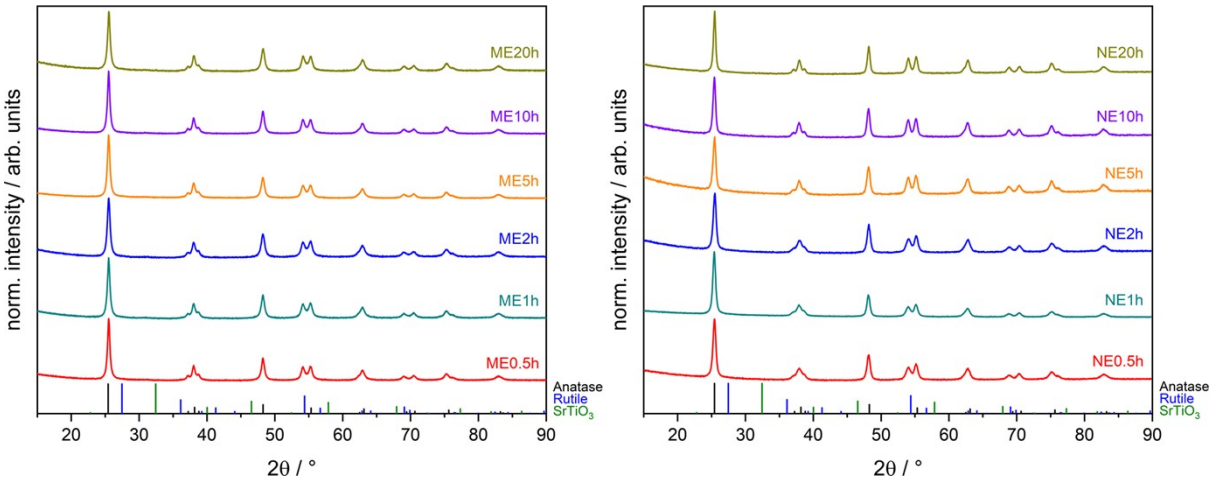


Figure S8: XRD patterns of the ME and NE series.

Table S6: Crystallite sizes (nm) of the ME series.

| phase | ME0.5h | ME1h | ME2h | ME5h | ME10h | ME20h |
|---|---|---|---|---|---|---|
| $TiO_2$ | 20 | 20 | 19 | 20 | 20 | 20 |

Table S7: Crystallite sizes (nm) of the NE series.

| phase | NE0.5h | NE1h | NE2h | NE5h | NE10h | NE20h |
|---|---|---|---|---|---|---|
| $TiO_2$ | 18 | 19 | 18 | 18 | 20 | 23 |

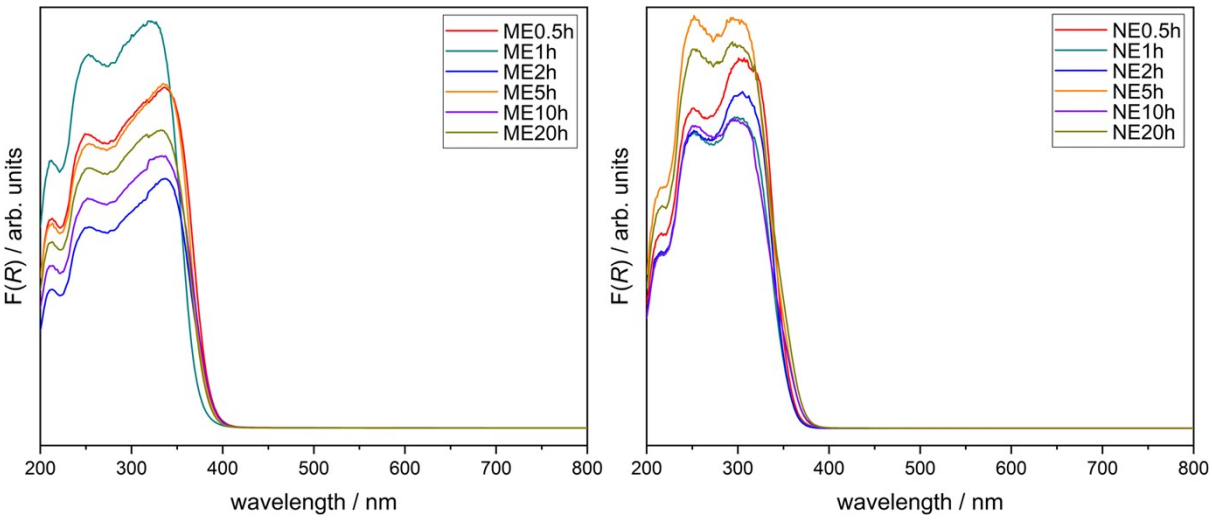


Figure S9: Kubelka-Munk plots of the ME and NE series.

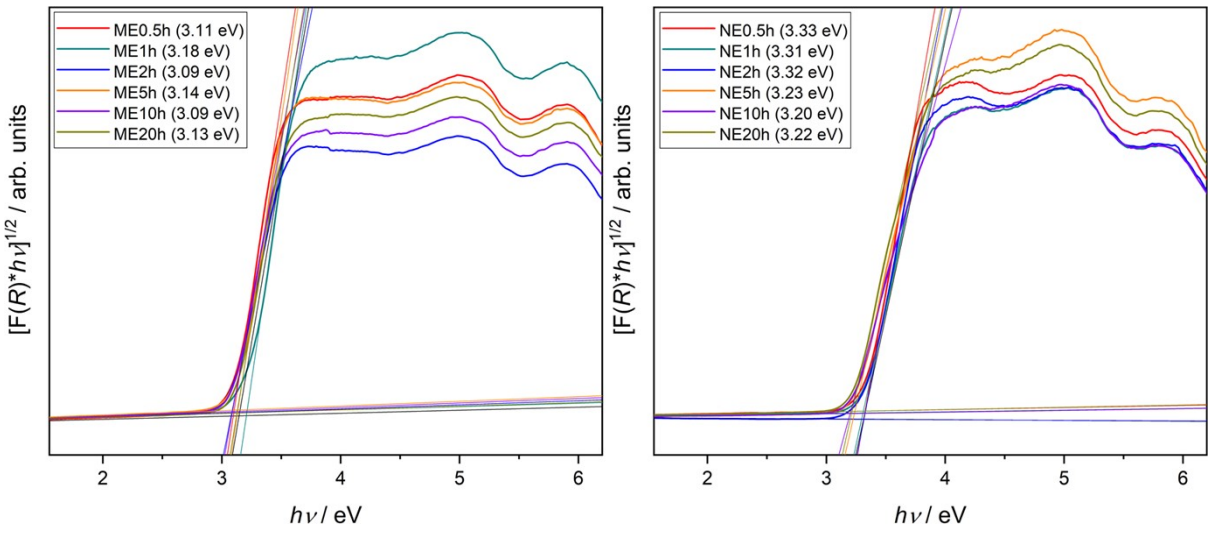


Figure S10: Tauc plots of the ME and NE series.

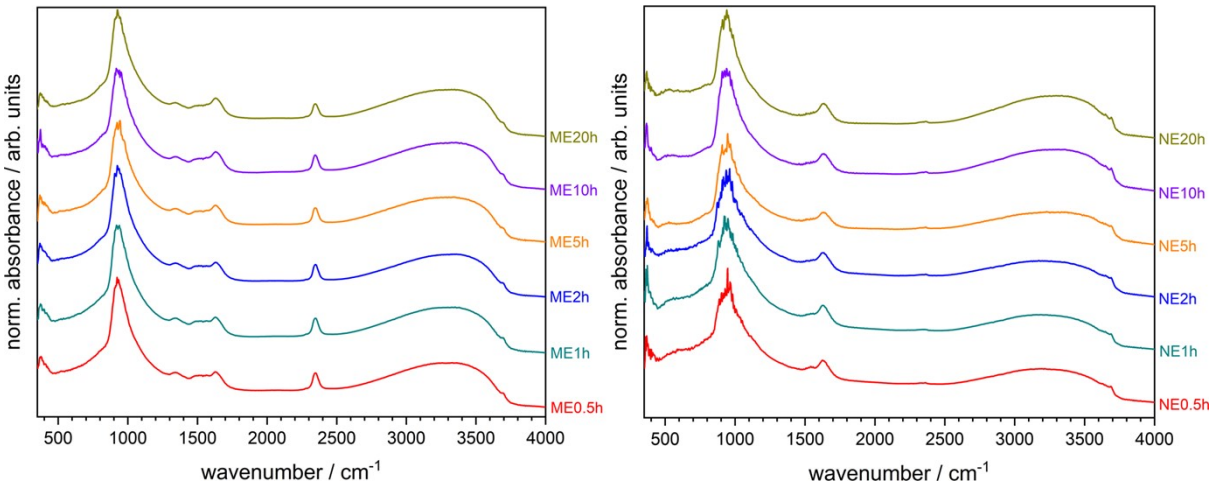


Figure S11: DRIFT spectra of the ME and NE series.

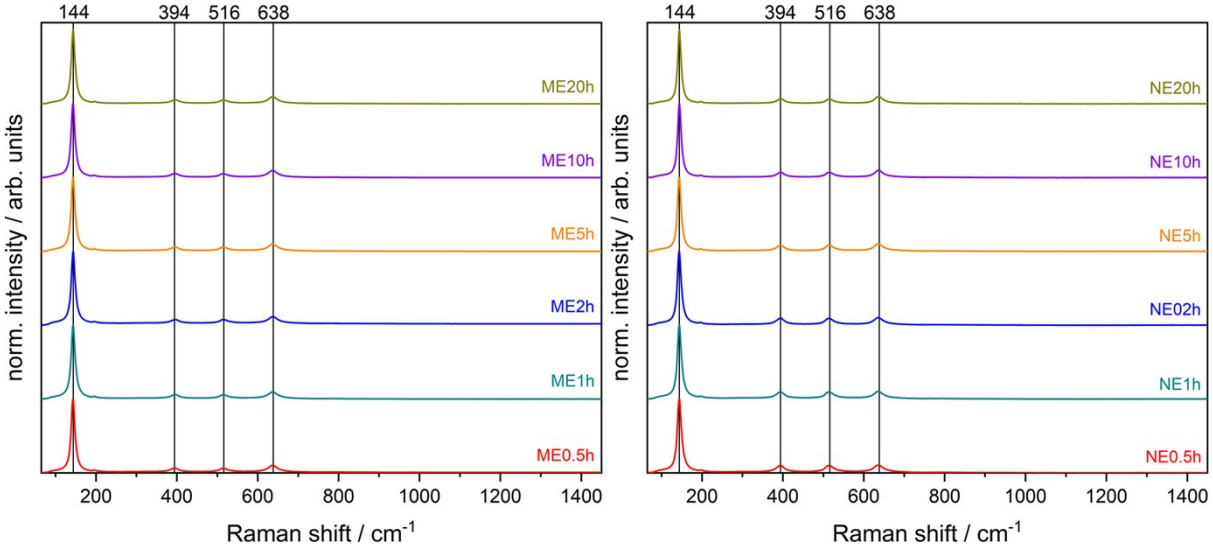


Figure S12: Raman spectra of the ME and NE series.

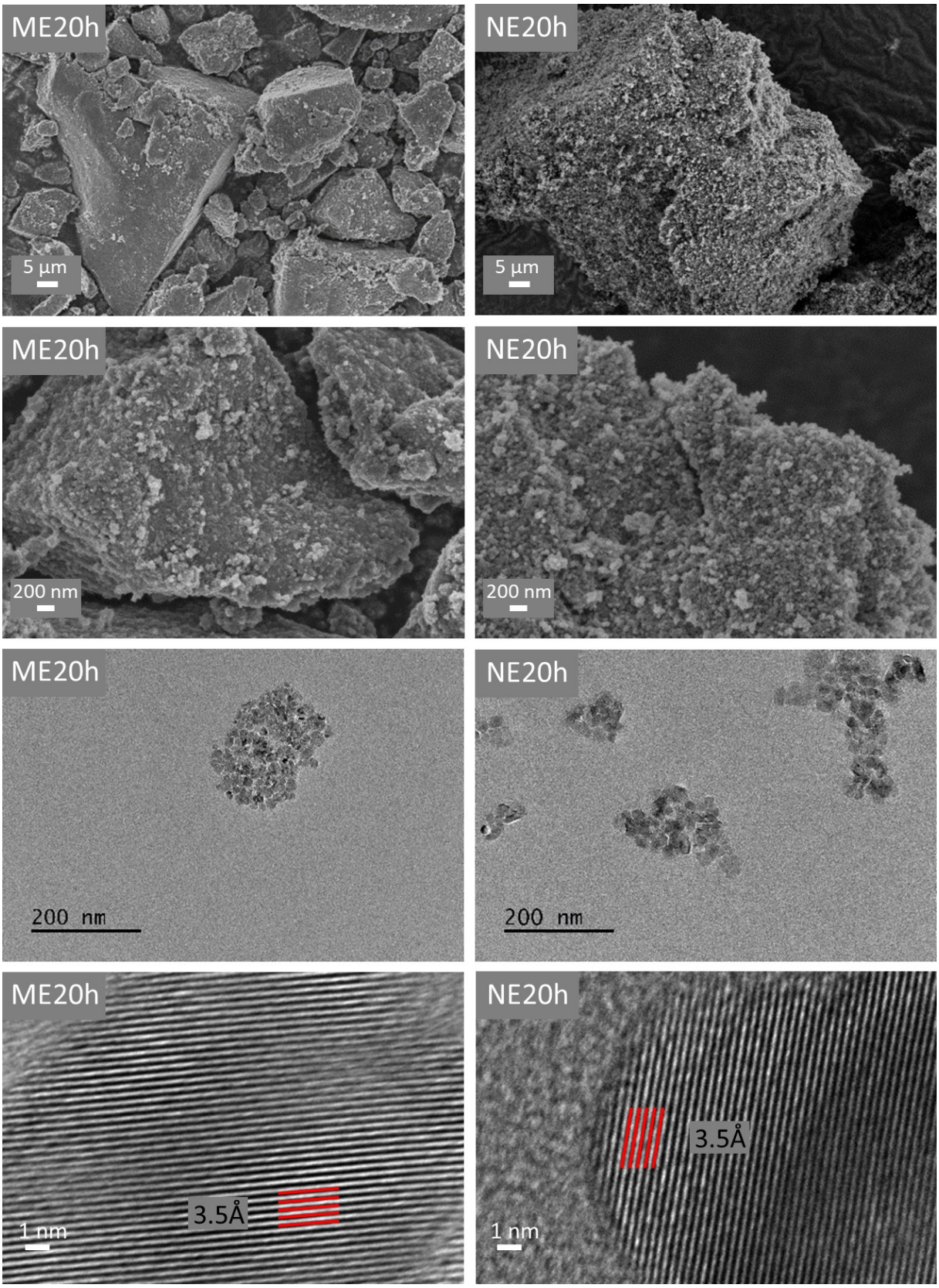


Figure S13: SEM images (top) and TEM images (bottom) of ME20h (left) and NE20h (right).

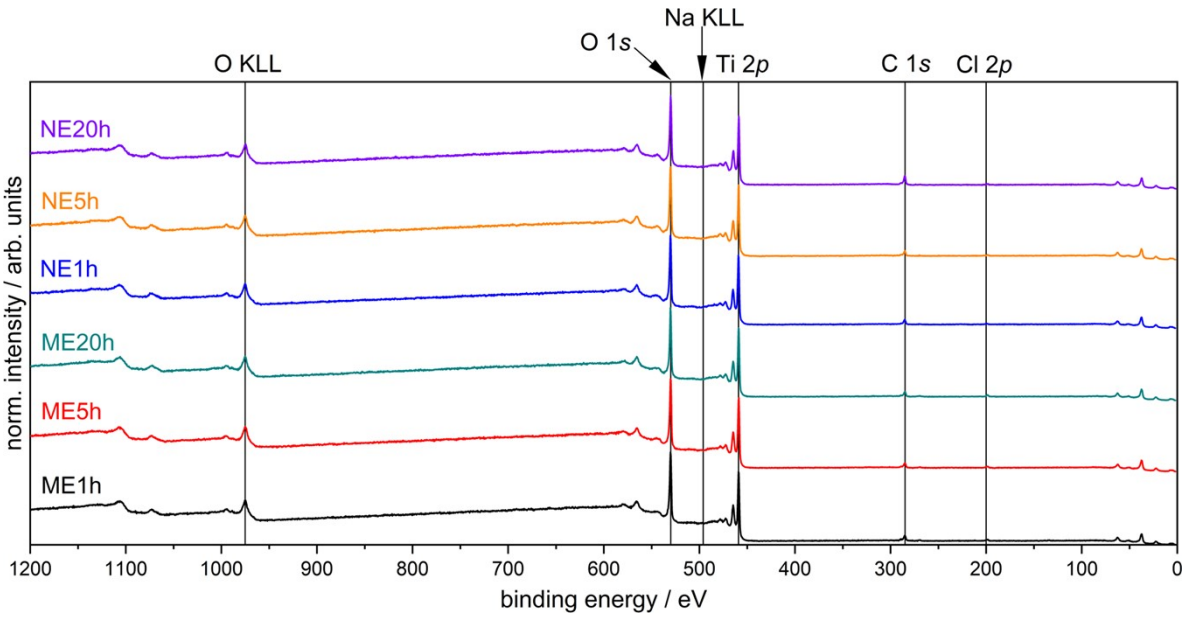


Figure 14: XP survey spectra of selected samples from the ME and NE series.

Table S8: Atomic percentages (at%) of selected samples from the ME and NE series obtained from XP survey spectra.

| sample | C 1*s* | Sr 3*d* | Ti 2*p* | O 1*s* | Na 1*s* | Cl 2*p* |
|---|---|---|---|---|---|---|
| ME1h | 14.08 | - | 24.31 | 60.54 | - | 1.07 |
| ME5h | 12.75 | - | 25.05 | 61.17 | - | 1.03 |
| ME20h | 12.51 | - | 24.24 | 62.04 | - | 1.20 |
| NE1h | 13.29 | - | 24.54 | 61.60 | - | 0.57 |
| NE5h | 11.84 | - | 25.37 | 61.79 | - | 1.00 |
| NE20h | 20.87 | - | 22.10 | 56.49 | - | 0.54 |

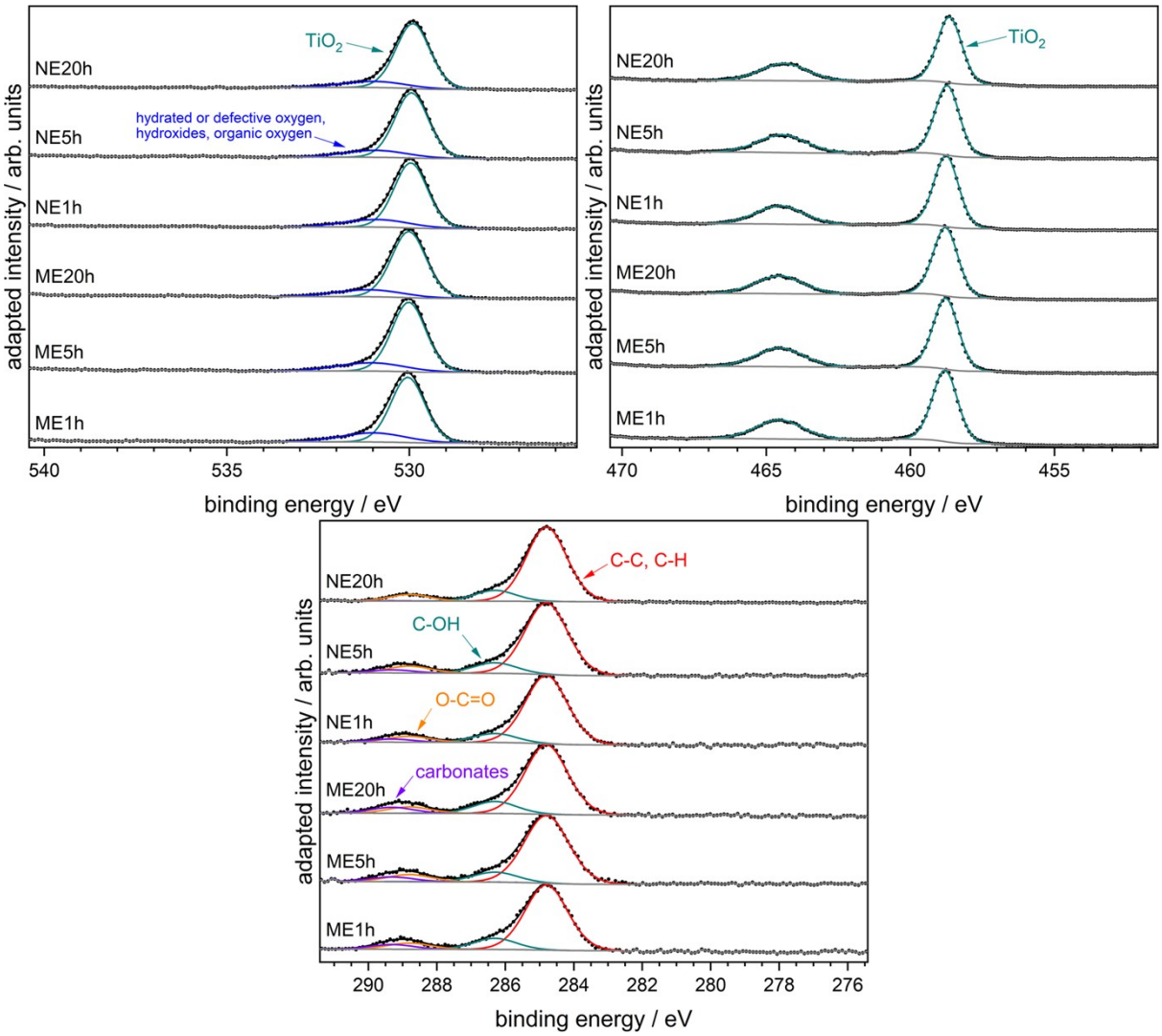


Figure S15: High-resolution XP spectra of selected samples from the ME and NE series (top left: O 1*s*; top right: Ti 2*p*; bottom: C 1*s*).

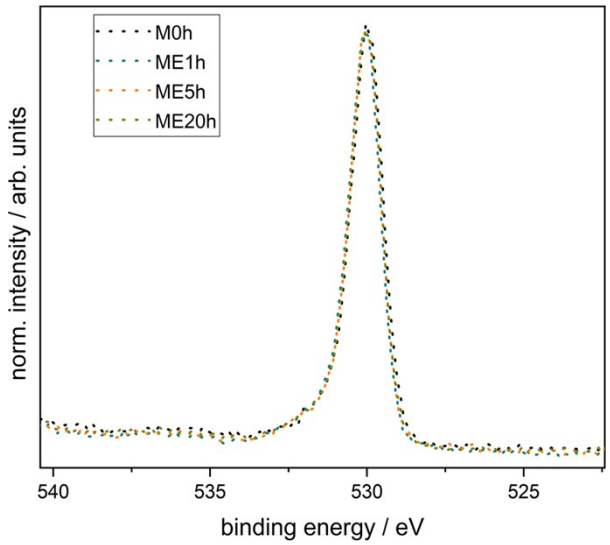


Figure S16: Overlaid O 1*s* spectra of selected samples from the ME series.

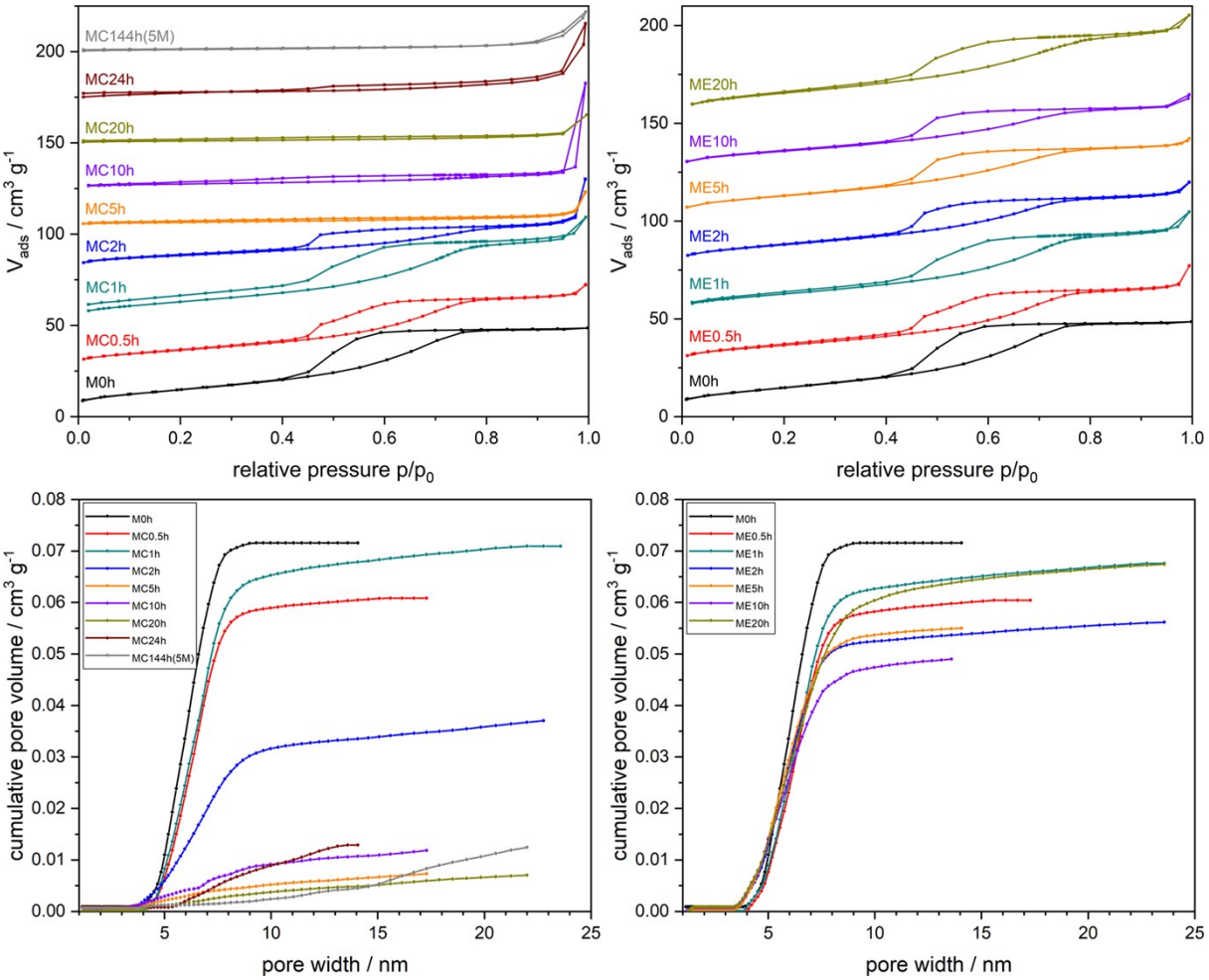


Figure S17: $N_2$ physisorption isotherms (top) and cumulative pore volumes (bottom) of the MC series (left) and ME series (right). Isotherms are shifted by 25 cm$^3$ g$^{-1}$, respectively.

Table S9: BET surface areas and cumulative pore volumes of the MC and ME series.

| sample | M0h | MC0.5h | MC1h | MC2h | MC5h | MC10h | MC20h | MC24h | MC144h(5M) |
|---|---|---|---|---|---|---|---|---|---|
| BET surface area [$m^2/g$] | 54.2 (average) | 42.7 | 48.0 | 42.0 | 5.8 | 9.1 | 4.1 | 9.1 | 5.3 |
| cumu-lative pore volume [$cm^3/g$] | 0.072 | 0.061 | 0.071 | 0.037 | 0.007 | 0.012 | 0.007 | 0.013 | 0.012 |
| sample | - | ME0.5h | ME1h | ME2h | ME5h | ME10h | ME20h | - | - |
| BET surface area [$m^2/g$] | - | 43.4 | 47.3 | 44.1 | 47.8 | 40.7 | 56.4 | - | - |
| cumu-lative pore volume [$cm^3/g$] | - | 0.060 | 0.068 | 0.056 | 0.055 | 0.049 | 0.067 | - | - |

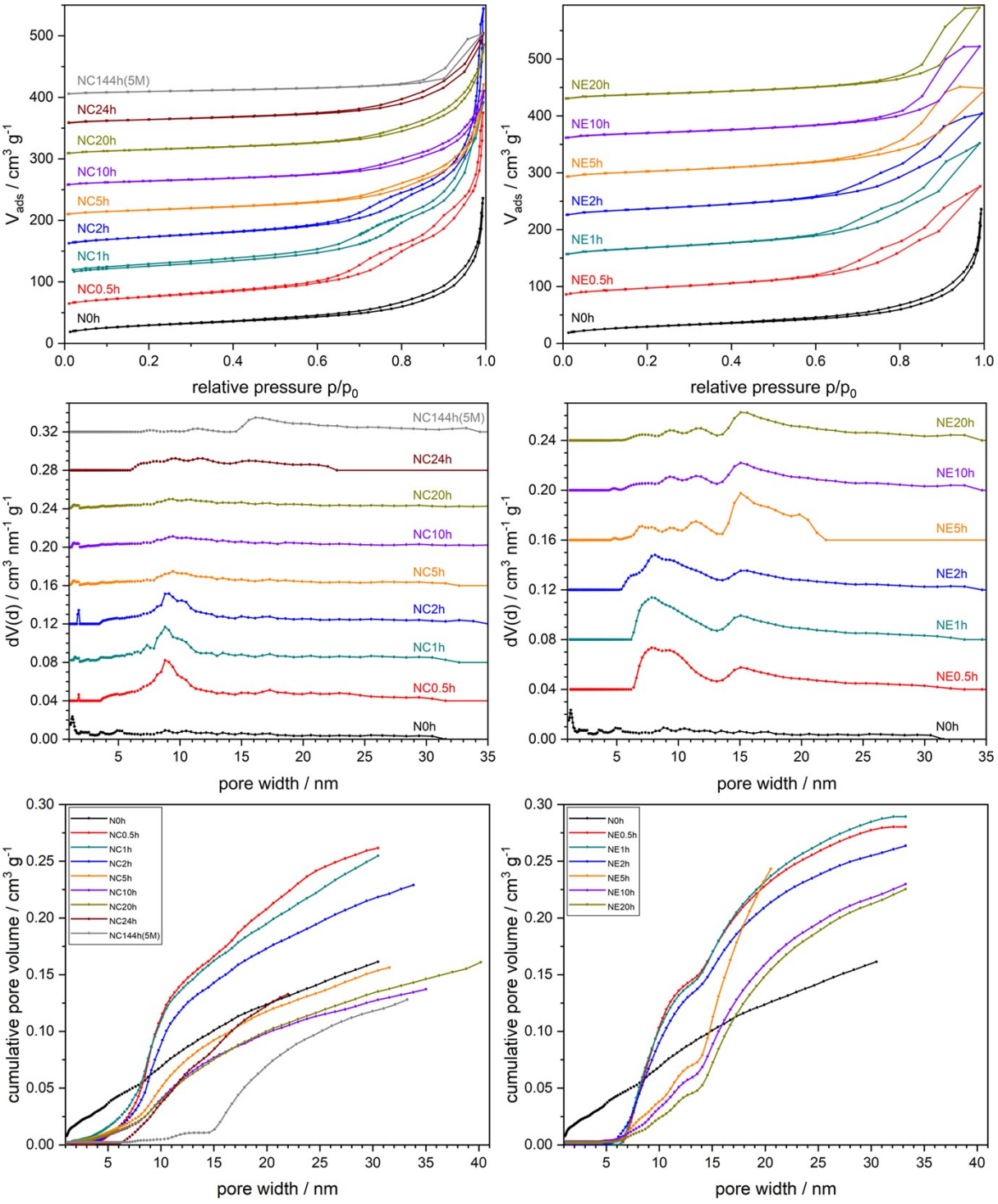


Figure S18: $N_2$ physisorption isotherms (top), pore size distributions (middle), and cumulative pore volumes (bottom) of the NC series (left) and NE series (right). Isotherms are shifted by 50 cm$^3$ g$^{-1}$ (NC series) and 70 cm$^3$ g$^{-1}$ (NE series), respectively. Pore size distributions are shifted by 0.04 cm$^3$ nm$^{-1}$ g$^{-1}$, respectively.

Table S10: BET surface areas and cumulative pore volumes of the NC and NE series.

| sample | N0h | NC0.5h | NC1h | NC2h | NC5h | NC10h | NC20h | NC24h | NC144h(5M) |
|---|---|---|---|---|---|---|---|---|---|
| BET surface area [$m^2/g$] | 97.4 | 94.2 | 92.5 | 84.2 | 60.9 | 50.0 | 53.8 | 48.7 | 33.0 |
| cumulative pore volume [$cm^3/g$] | 0.161 | 0.261 | 0.255 | 0.229 | 0.156 | 0.137 | 0.161 | 0.133 | 0.128 |
| sample | - | NE0.5h | NE1h | NE2h | NE5h | NE10h | NE20h | - | - |
| BET surface area [$m^2/g$] | - | 97.1 | 98.7 | 95.0 | 80.0 | 69.8 | 63.7 | - | - |
| cumulative pore volume [$cm^3/g$] | - | 0.280 | 0.289 | 0.264 | 0.243 | 0.230 | 0.225 | - | - |

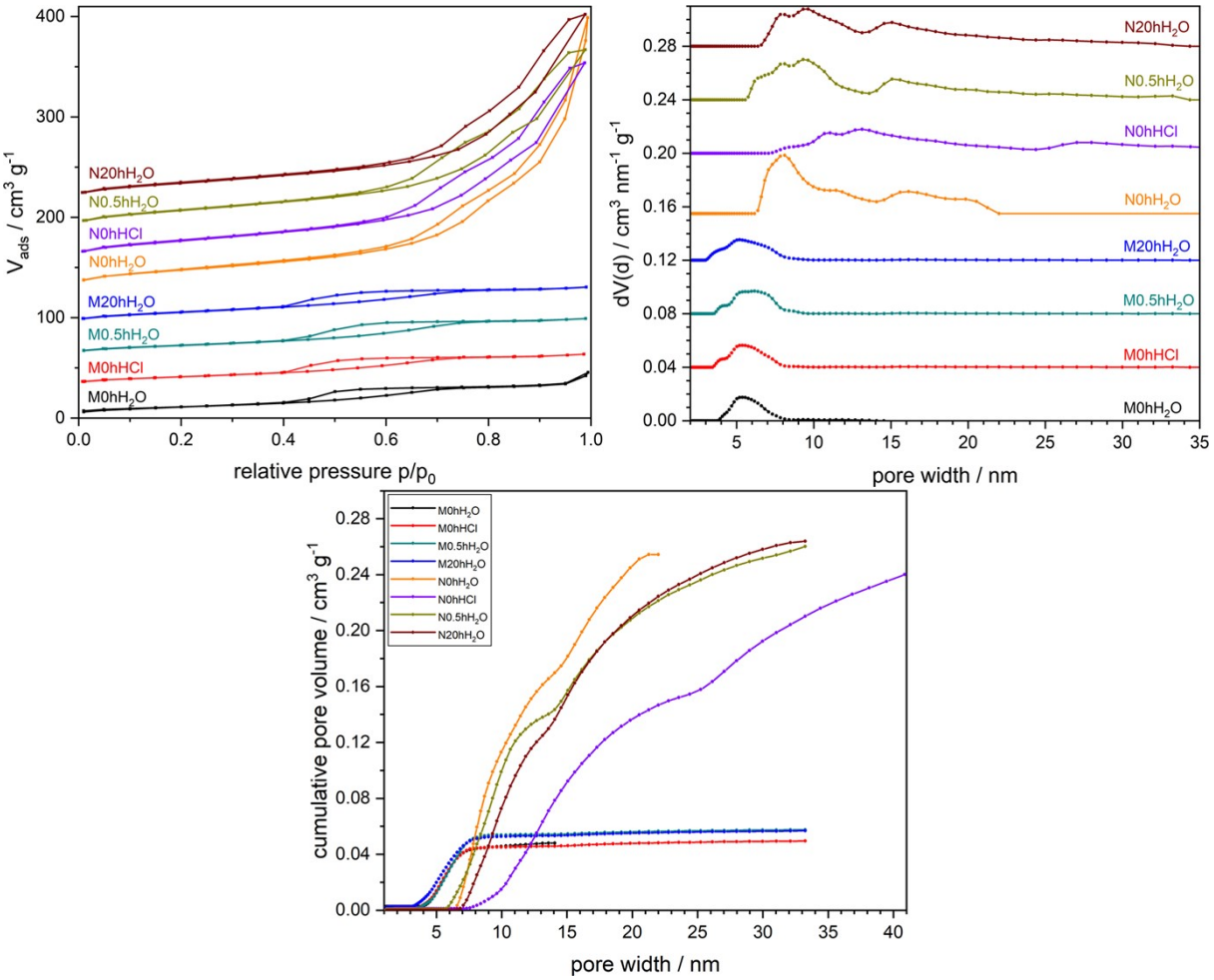


Figure S19: $N_2$ physisorption isotherms (left), pore size distributions (right), and cumulative pore volumes (bottom) of mesoporous and nanoparticulate control samples ($H_2O$ work-up, HCl work-up, and $H_2O$ treatment). Isotherms are shifted by 30 $cm^3\ g^{-1}$, respectively. Pore size distributions are shifted by 0.04 $cm^3\ nm^{-1}\ g^{-1}$, respectively.

Table S11: BET surface areas and cumulative pore volumes of mesoporous and nanoparticulate samples ($H_2O$ work-up, HCl work-up, and $H_2O$ treatment).

| sample | M0h$H_2O$ | M0hHCl | M0.5h$H_2O$ | M20h$H_2O$ |
|---|---|---|---|---|
| BET surface area [$m^2/g$] | 39.9 | 40.7 | 45.3 | 55.9 |
| cumulative pore volume [$cm^3/g$] | 0.048 | 0.050 | 0.058 | 0.059 |
| sample | N0h$H_2O$ | N0hHCl | N0.5h$H_2O$ | N20h$H_2O$ |
| BET surface area [$m^2/g$] | 97.4 | 96.1 | 96.7 | 86.7 |
| cumulative pore volume [$cm^3/g$] | 0.254 | 0.273 | 0.260 | 0.264 |

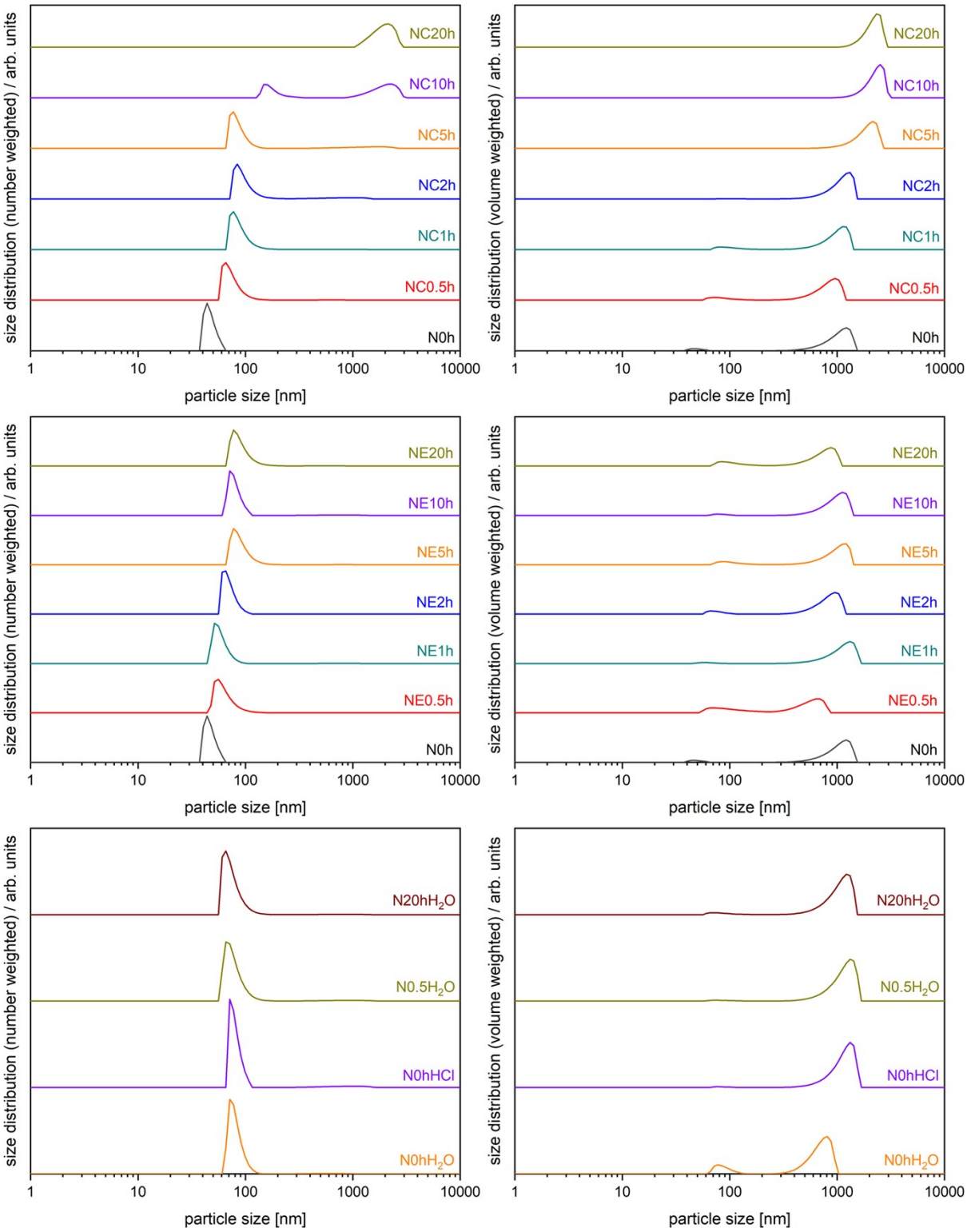


Figure S20: Number weighted particle size distributions (left) and volume weighted particle size distributions (right) of hydrothermally converted nanoparticles (NC series, top), hydrothermally etched nanoparticles (NE series, middle), and nanoparticulate control samples (bottom) determined by DLS.

Table S12: Maxima of number and volume weighted size distributions of nanoparticulate samples determined by DLS.

| sample | maxima | maxima | sample | maxima | maxima | sample | maxima | maxima |
|---|---|---|---|---|---|---|---|---|

| | number weighted size distribution [nm] | volume weighted size distribution [nm] | | number weighted size distribution [nm] | number weighted size distribution [nm] | | number weighted size distribution [nm] | volume weighted size distribution [nm] |
|---|---|---|---|---|---|---|---|---|
| N0h | 44 | 48/ 1216 | - | - | - | N0h$H_2O$ | 71 | 77/ 811 |
| NC0.5h | 66 | 71/ 954 | NE0.5h | 56 | 71/ 690 | N0hHCl | 71 | 77/ 1319 |
| NC1h | 77 | 84/ 1216 | NE1h | 52 | 56/ 1319 | N0.5h$H_2O$ | 66 | 1319 |
| NC2h | 84 | 1318 | NE2h | 66 | 66/ 954 | N20h$H_2O$ | 66 | 71/ 1216 |
| NC5h | 77 | 2144 | NE5h | 77 | 84/ 1216 | - | - | - |
| NC10h | 148/ 2144 | 2521 | NE10h | 71 | 77/ 1121 | - | - | - |
| NC20h | 2144 | 2325 | NE20h | 77 | 84/ 880 | - | - | - |

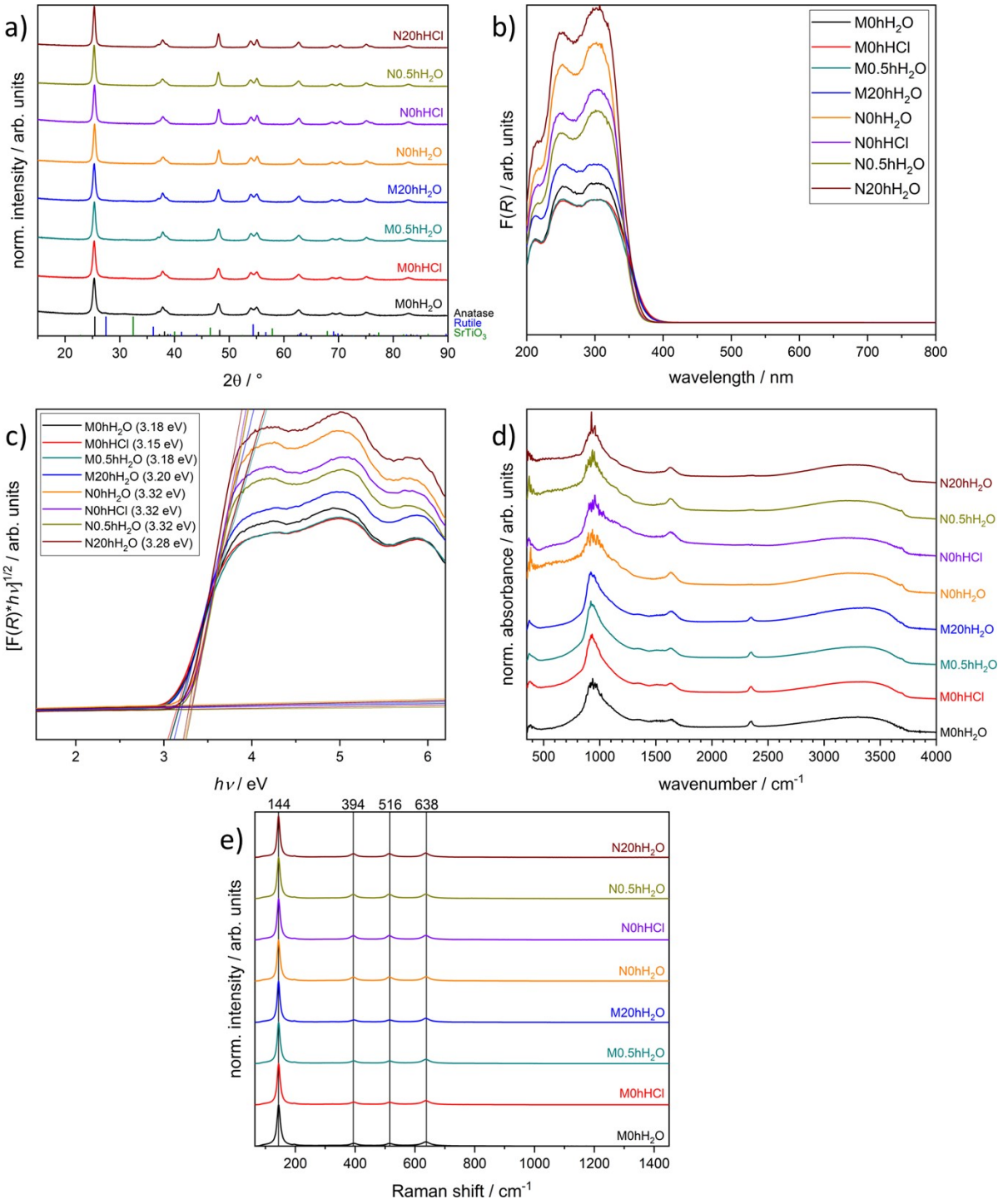


Figure S21: XRD patterns (a), Kubelka-Munk plots (b), Tauc plots (c), DRIFT spectra (d), and Raman spectra (e) of mesoporous and nanoparticulate control samples ($H_2O$ work-up, HCl work-up, and $H_2O$ treatment).

Table S13: Crystallite sizes (nm) of mesoporous and nanoparticulate control samples ($H_2O$ work-up, HCl work-up, and $H_2O$ treatment).

| phase | M0h$H_2O$ | M0hHCl | M0.5h$H_2O$ | M20h$H_2O$ | N0h$H_2O$ | N0hHCl | N0.5h$H_2O$ | N20h$H_2O$ |
|---|---|---|---|---|---|---|---|---|
| $TiO_2$ | 17 | 17 | 17 | 17 | 18 | 18 | 19 | 19 |

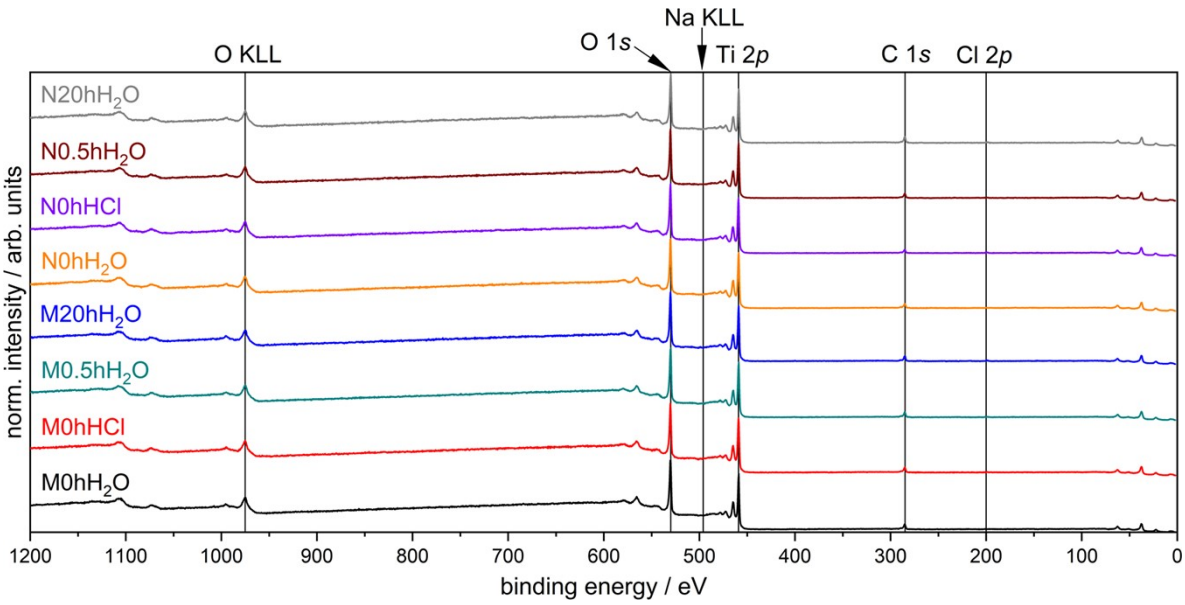


Figure S22: XP survey spectra of mesoporous and nanoparticulate control samples ($H_2O$ work-up, HCl work-up, and $H_2O$ treatment).

Table S14: Atomic percentages (at%) of mesoporous and nanoparticulate control samples ($H_2O$ work-up, HCl work-up, and $H_2O$ treatment) obtained from XP survey spectra.

| sample | C 1*s* | Sr 3*d* | Ti 2*p* | O 1*s* | Na 1*s* | Cl 2*p* |
|---|---|---|---|---|---|---|
| M0hH$_2$O | 15.30 | - | 24.02 | 60.68 | - | - |
| M0hHCl | 15.31 | - | 24.21 | 60.22 | - | 0.26 |
| M0.5hH$_2$O | 15.47 | - | 24.02 | 59.93 | - | 0.59 |
| M20hH$_2$O | 16.97 | - | 23.88 | 58.49 | - | 0.66 |
| N0hH$_2$O | 15.49 | - | 25.45 | 59.06 | - | - |
| N0hHCl | 10.49 | - | 25.38 | 63.24 | - | 0.56 |
| N0.5hH$_2$O | 16.54 | - | 24.83 | 58.15 | - | 0.48 |
| N20hH$_2$O | 16.88 | - | 23.83 | 58.56 | - | 0.72 |

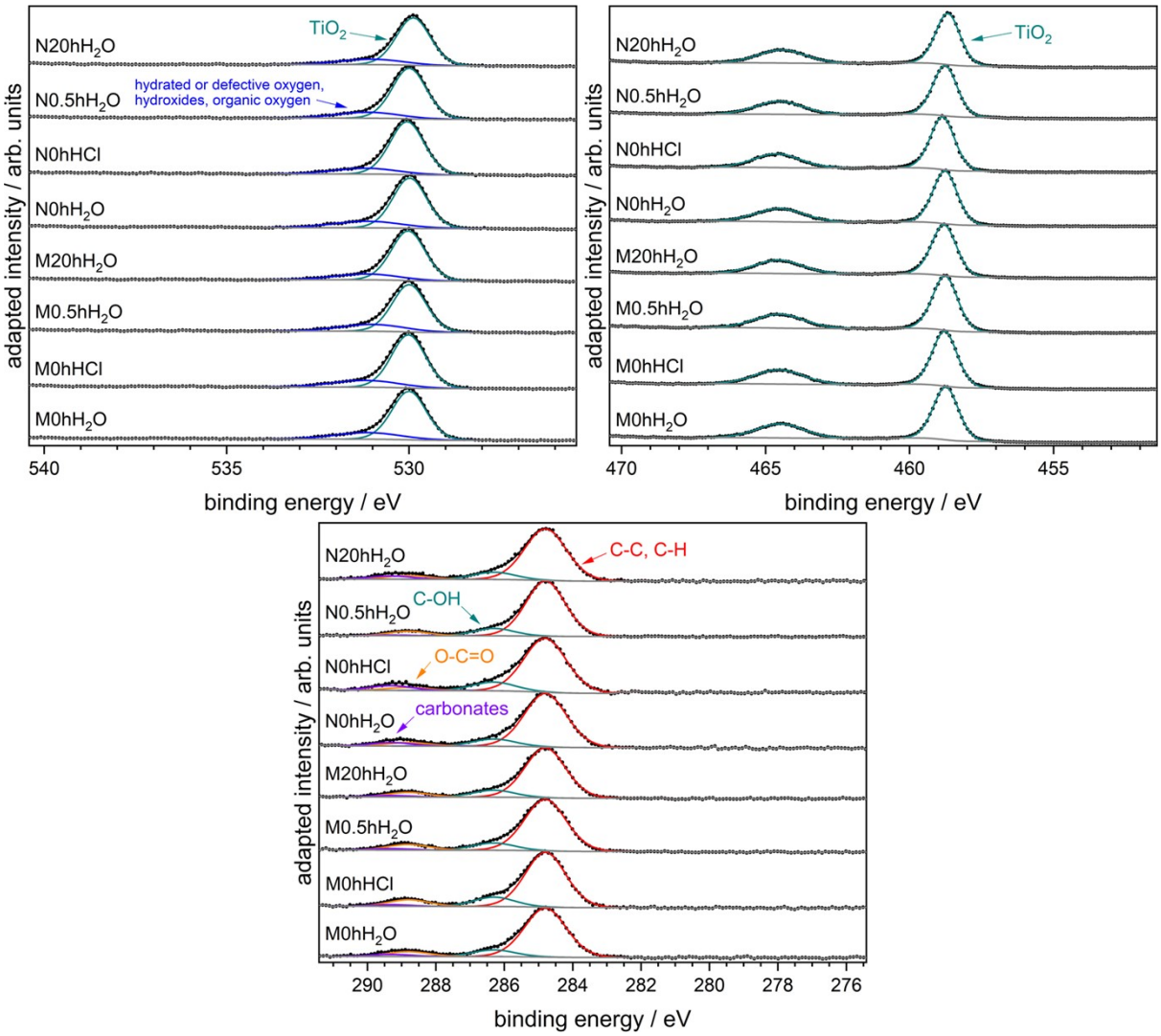


Figure S23: High-resolution XP spectra of mesoporous and nanoparticulate control samples (top left: O 1*s*; top right: Ti 2*p*; bottom: C 1*s*).

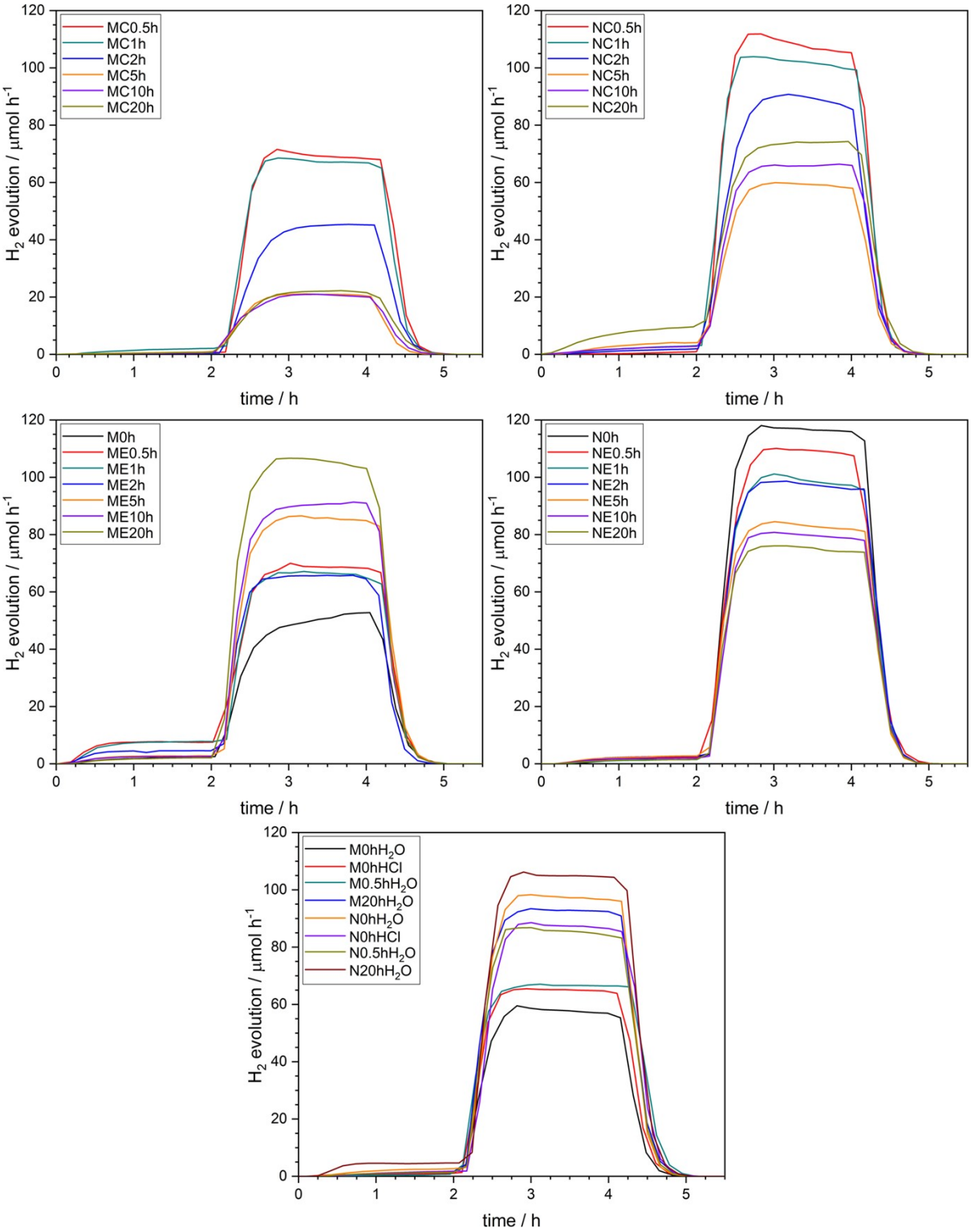


Figure S24: Photocatalytic $H_2$ evolution under simulated solar light irradiation of all samples (up to 20 h reaction time). Co-catalyst photodeposition (0.1 wt% Pt) was performed after 2 h.

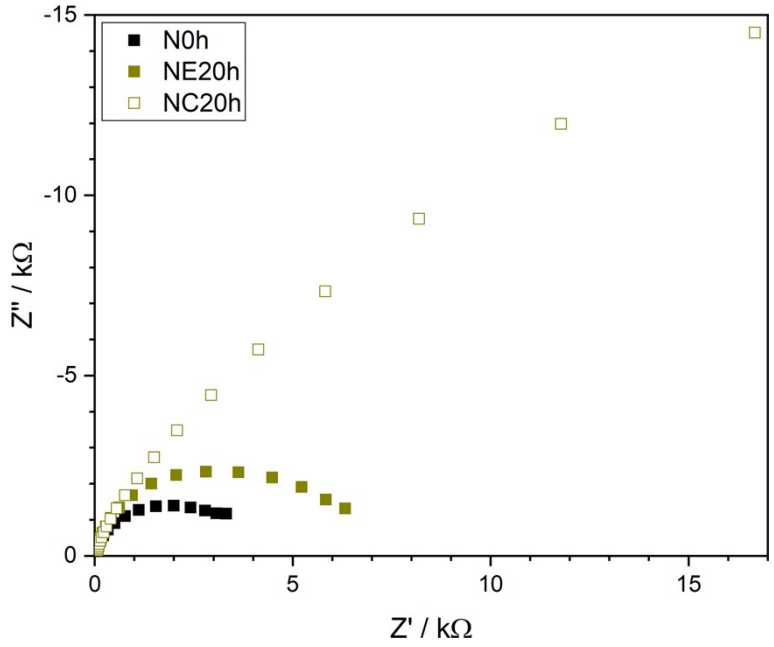


Figure S25: Nyquist plots of photoelectrodes under simulated solar light irradiation.

Post photocatalysis (HER):

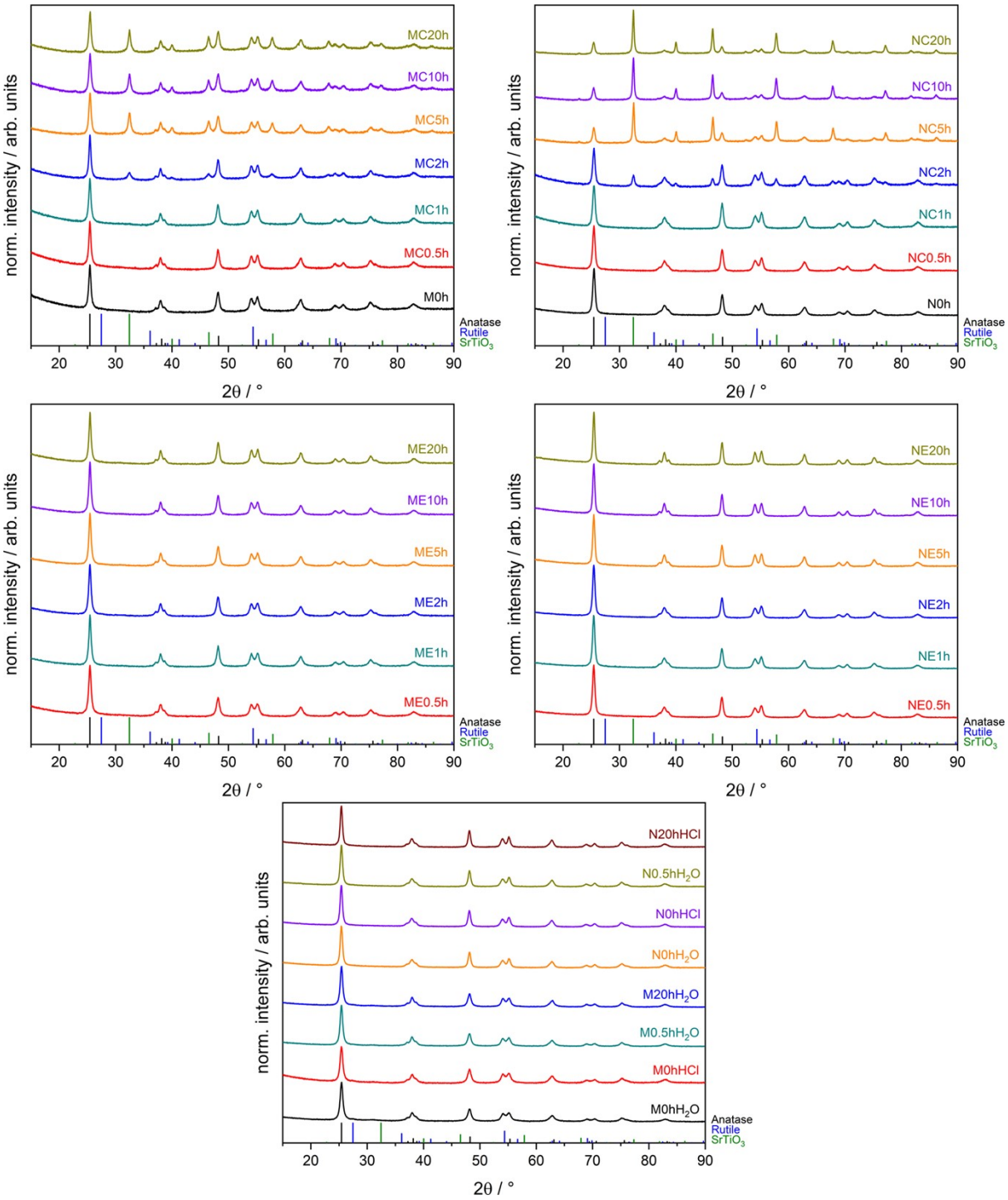


Figure S26: XRD patterns of the MC series (top left), NC series (top right), ME series (middle left), NE series (middle right), and control experiments (bottom) after photocatalytic $H_2$ evolution experiments.

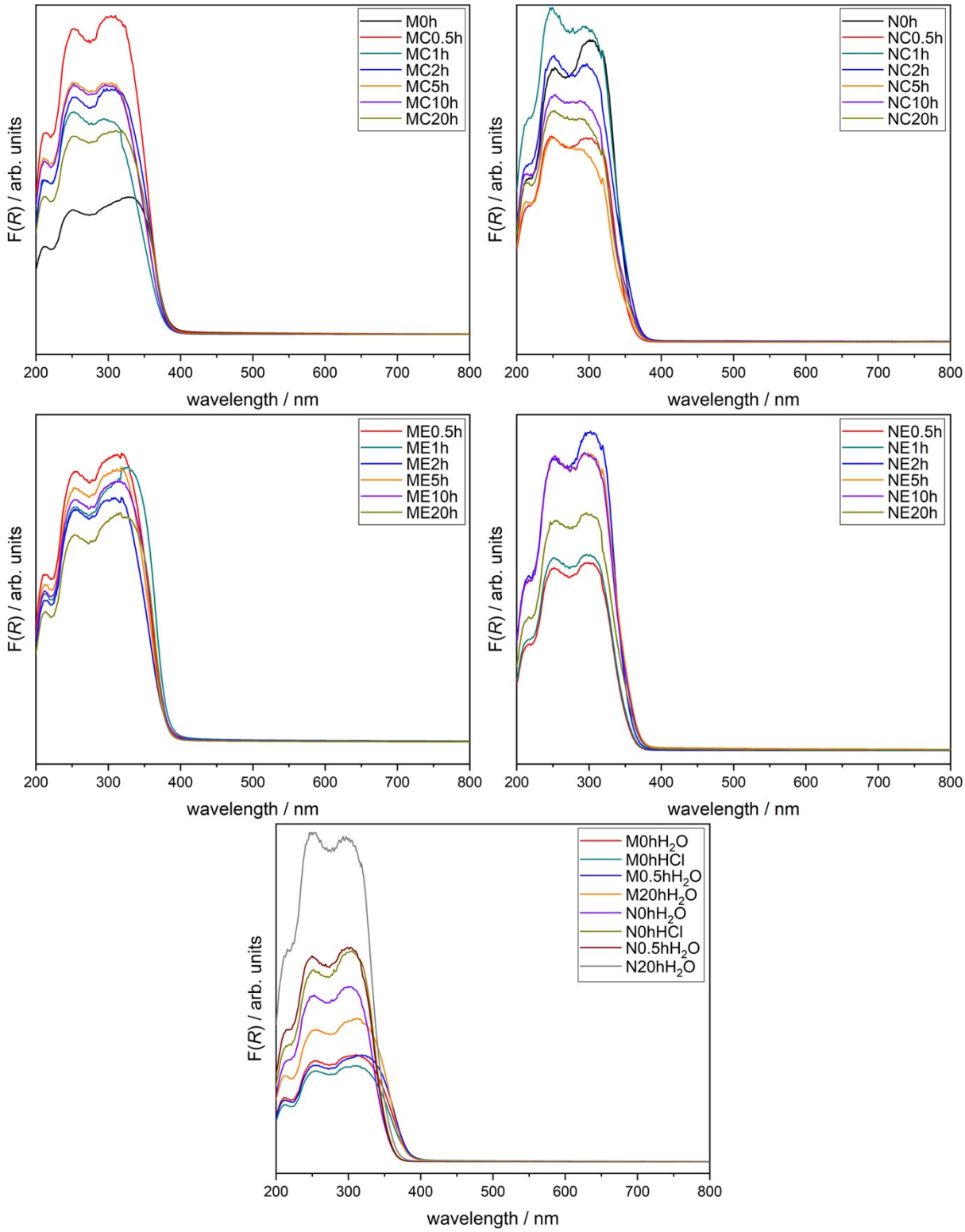


Figure S27: Kubelka-Munk plots of converted (top), etched (middle), and control samples (bottom) after photocatalytic $H_2$ evolution experiments.

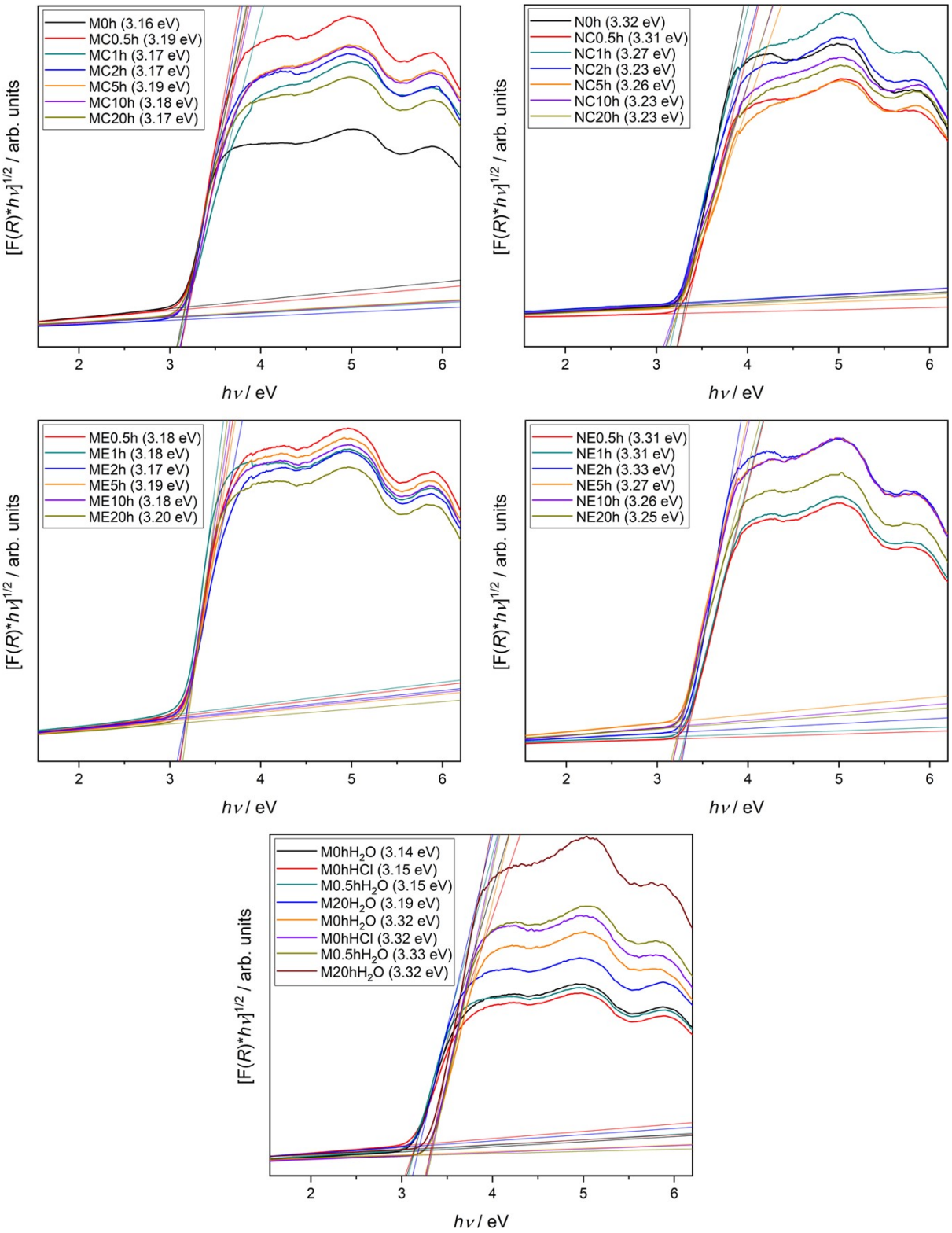


Figure S28: Tauc plots of converted (top), etched (middle), and control samples (bottom) after photocatalytic $H_2$ evolution experiments. Steeper tangents of the background are the result of broad absorption of the Pt co-catalyst.

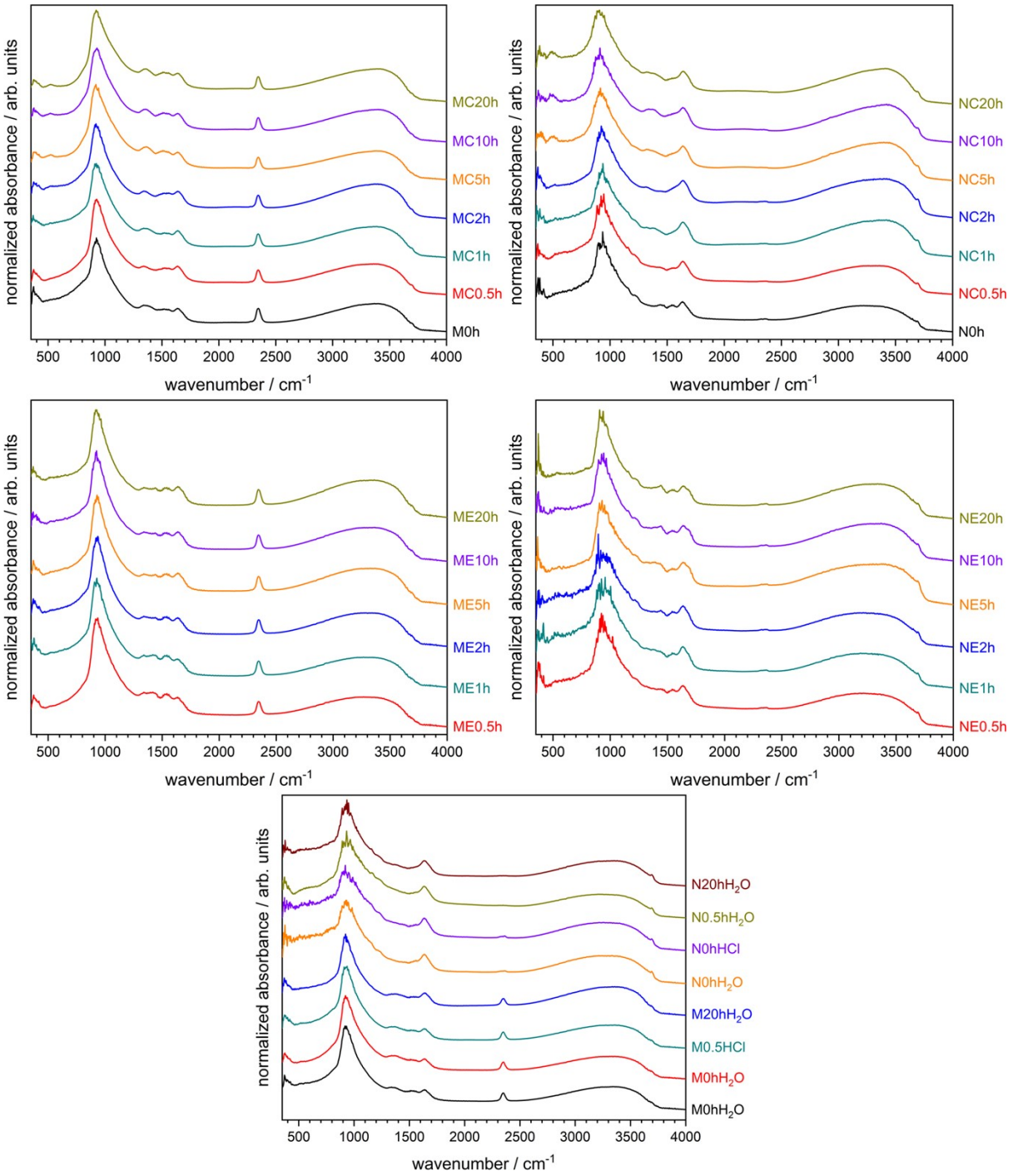


Figure S29: DRIFT spectra of converted (top), etched (middle), and control samples (bottom) after photocatalytic $H_2$ evolution experiments.

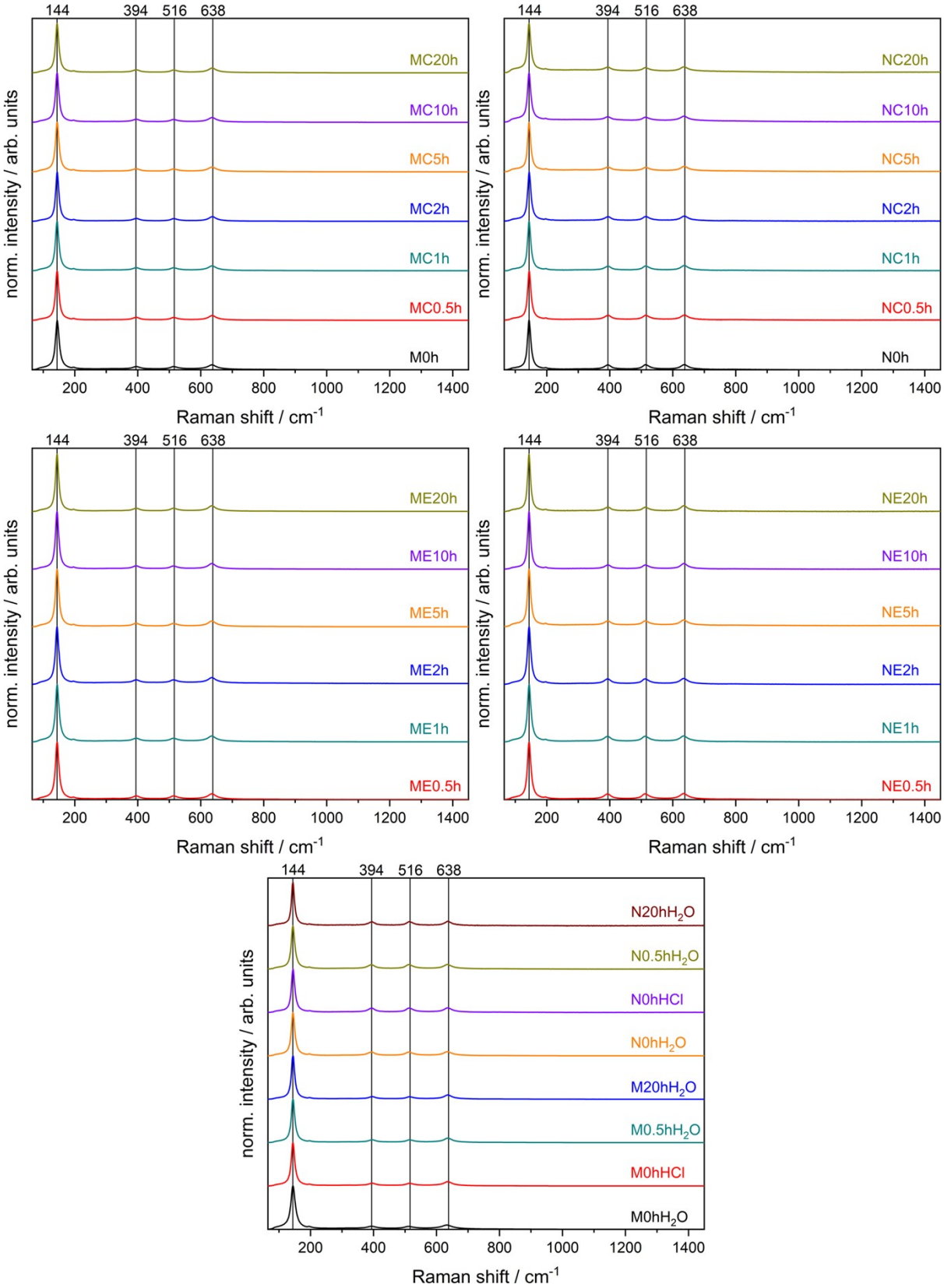


Figure S30: Raman spectra of converted (top), etched (middle), and control samples (bottom) after photocatalytic $H_2$ evolution experiments.

## $H_2O$ isotherms

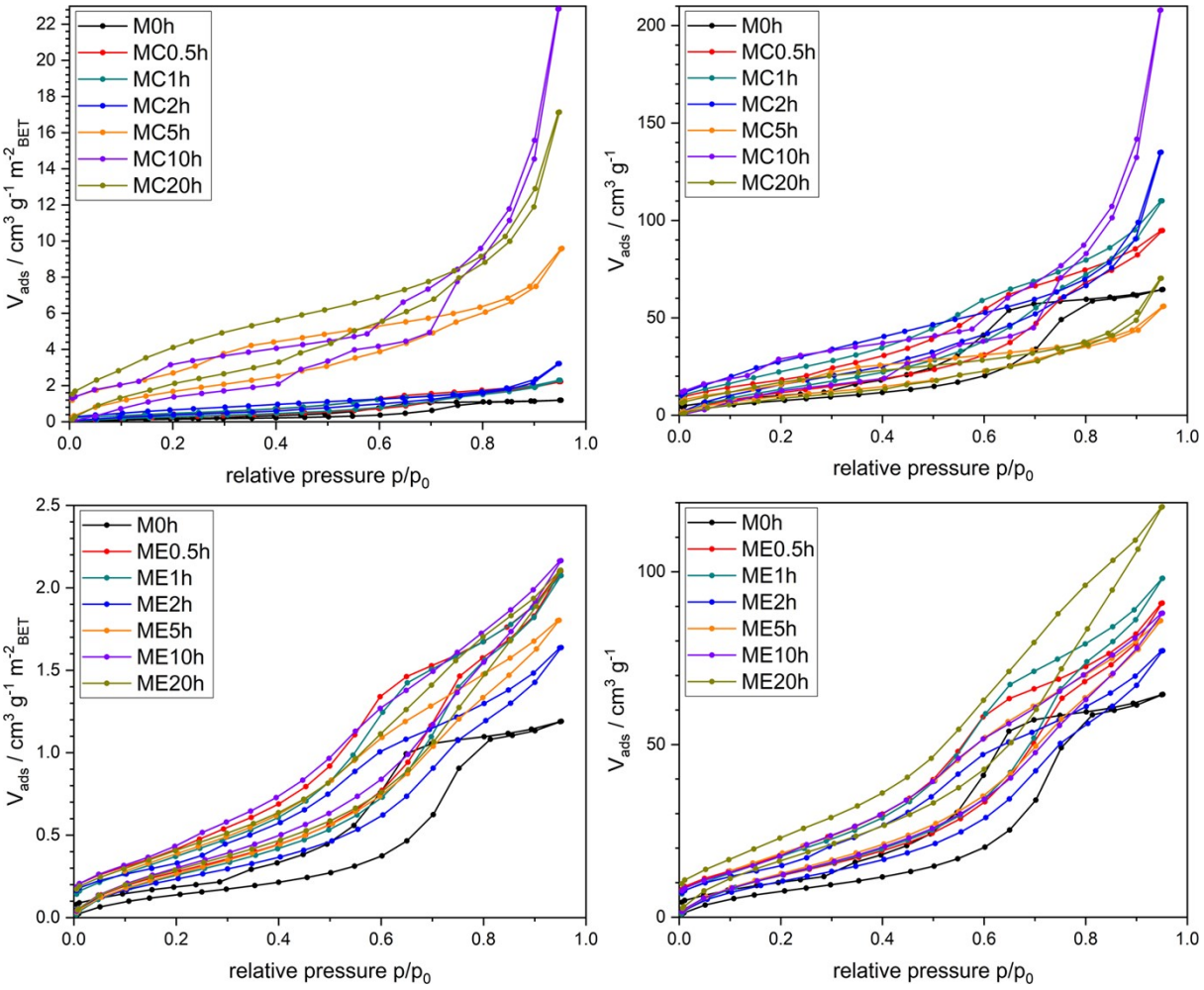


Figure S31: $H_2O$ physisorption isotherms of converted mesoporous samples (top) and etched mesoporous $TiO_2$ (bottom). Isotherms normalized by $N_2$ BET surface area are shown on the left and were derived from full isotherms depicted on the right.

Table S15: Normalized and measured adsorbed volumes of the MC and ME series at $p/p_0 = 0.3$.

| sample | $V_{ads}$ [cm$^3$ g$^{-1}$ m$^{-2}_{BET}$] | $V_{ads}$ [cm$^3$ g$^{-1}$] | sample | $V_{ads}$ [cm$^3$ g$^{-1}$ m$^{-2}_{BET}$] | $V_{ads}$ [cm$^3$ g$^{-1}$] |
|---|---|---|---|---|---|
| M0h | 0.17 | 9.37 | - | - | - |
| MC0.5h | 0.35 | 14.82 | ME0.5h | 0.36 | 15.58 |
| MC1h | 0.37 | 17.68 | ME1h | 0.34 | 15.87 |
| MC2h | 0.49 | 20.39 | ME2h | 0.30 | 13.24 |
| MC5h | 2.07 | 12.09 | ME5h | 0.35 | 16.55 |
| MC10h | 1.70 | 15.51 | ME10h | 0.40 | 16.11 |
| MC20h | 2.65 | 10.87 | ME20h | 0.38 | 21.31 |

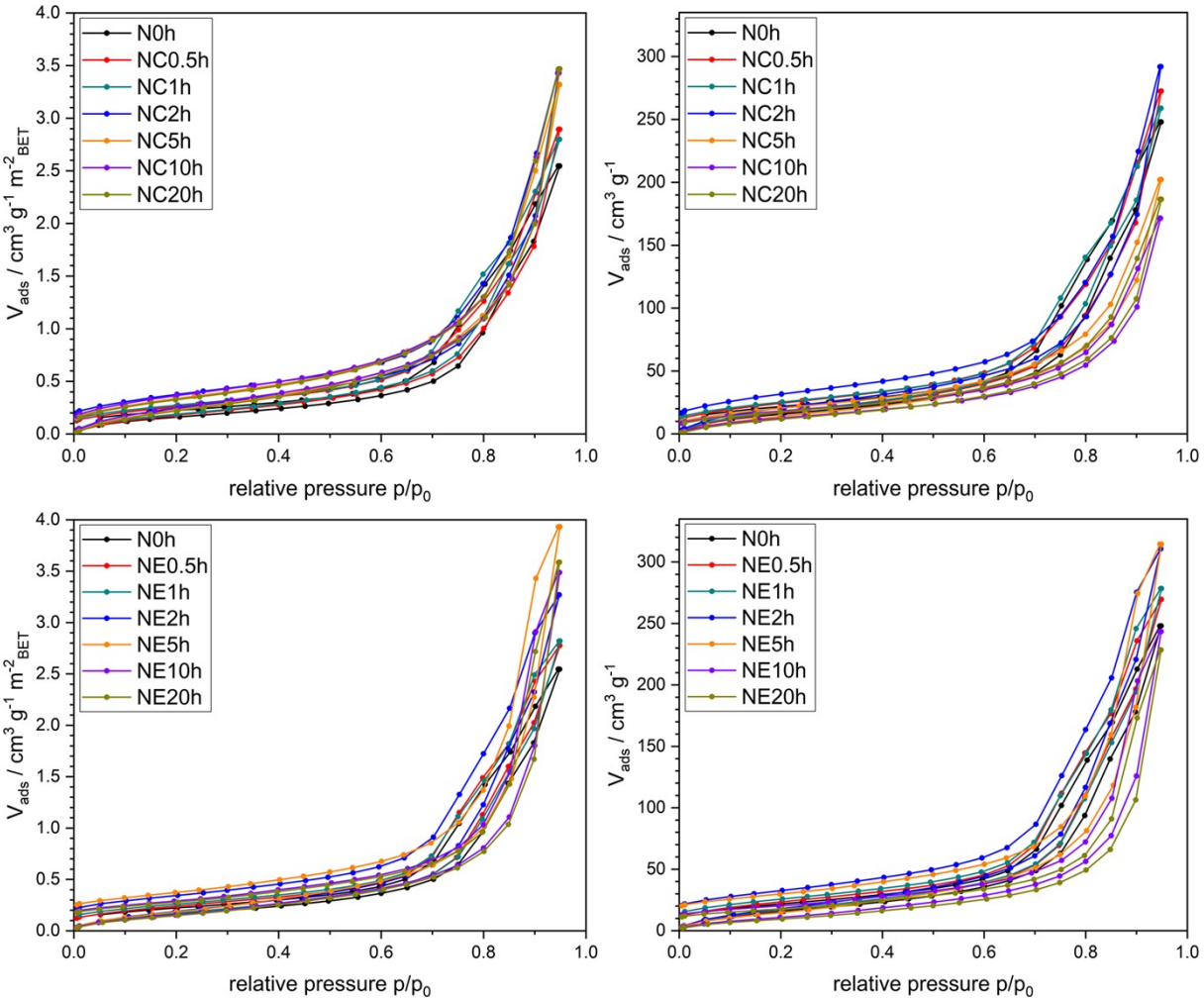


Figure S32: $H_2O$ physisorption isotherms of converted nanoparticles (top) and etched $TiO_2$ nanoparticles (bottom). Isotherms normalized by $N_2$ BET surface area are shown on the left and were derived from full isotherms depicted on the right.

Table S16: Normalized and measured adsorbed volumes of the NC and NE series at $p/p_0 = 0.3$.

| sample | $V_{ads}$ [$cm^3\ g^{-1}\ m^{-2}_{BET}$] | $V_{ads}$ [$cm^3\ g^{-1}$] | sample | $V_{ads}$ [$cm^3\ g^{-1}\ m^{-2}_{BET}$] | $V_{ads}$ [$cm^3\ g^{-1}$] |
|---|---|---|---|---|---|
| N0h | 0.20 | 19.29 | - | - | - |
| NC0.5h | 0.23 | 21.62 | NE0.5h | 0.22 | 21.27 |
| NC1h | 0.24 | 21.75 | NE1h | 0.21 | 21.20 |
| NC2h | 0.31 | 25.88 | NE2h | 0.24 | 23.20 |
| NC5h | 0.29 | 17.94 | NE5h | 0.24 | 19.36 |
| NC10h | 0.32 | 16.13 | NE10h | 0.20 | 14.15 |
| NC20h | 0.29 | 15.50 | NE20h | 0.19 | 12.31 |

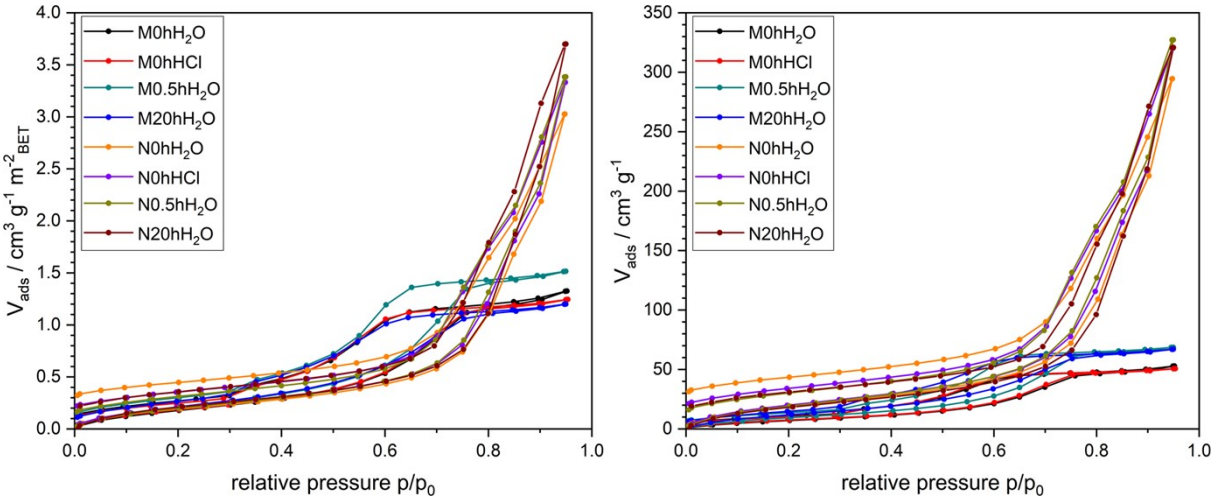


Figure S33: $H_2O$ physisorption isotherms of mesoporous and nanoparticulate control samples. Isotherms normalized by $N_2$ BET surface area are shown on the left and were derived from full isotherms depicted on the right.

Table S17: Normalized and measured adsorbed volumes of mesoporous and nanoparticulate control samples at $p/p_0 = 0.3$.

| sample | $V_{ads}$ [$cm^3\ g^{-1}\ m^{-2}_{BET}$] | $V_{ads}$ [$cm^3\ g^{-1}$] | sample | $V_{ads}$ [$cm^3\ g^{-1}\ m^{-2}_{BET}$] | $V_{ads}$ [$cm^3\ g^{-1}$] |
|---|---|---|---|---|---|
| $M0hH_2O$ | 0.23 | 9.20 | $N0hH_2O$ | 0.24 | 23.31 |
| M0hHCl | 0.23 | 9.46 | N0hHCl | 0.26 | 24.56 |
| $M0.5hH_2O$ | 0.27 | 12.15 | $N0.5hH_2O$ | 0.25 | 24.26 |
| $M20hH_2O$ | 0.28 | 15.40 | $N20hH_2O$ | 0.26 | 22.77 |

Long-term photocatalytic $H_2$ evolution measurement, literature comparison, and comparison of band edge positions

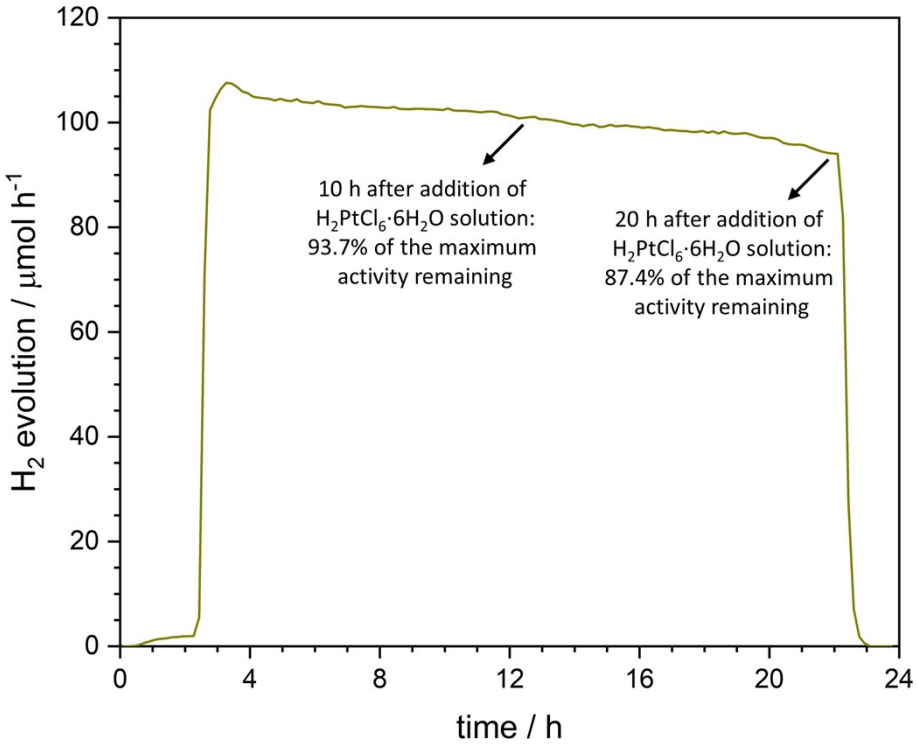


Figure S34: Long-term photocatalytic $H_2$ evolution of ME20h under simulated solar light irradiation. Co-catalyst photodeposition (0.1 wt% Pt) was performed after 2 h. The highest activity of 107.6 µmol $h^{-1}$ was measured approximately 1 h after the photodeposition.

Table S18: Comparison of photocatalytic $H_2$ evolution rates discussed in this work with literature results of different $SrTiO_3/TiO_2$ samples obtained by hydrothermal conversion of a $TiO_2$ starting materials. Stated $H_2$ evolution rates might deviate from values in the respective publications due back calculations from µmol $h^{-1}$ $g^{-1}$ to µmol $h^{-1}$.

| photo-catalyst | experimental conditions | co-catalyst | $H_2$ evolution [µmol $h^{-1}$] | percentage increase compared to $TiO_2$ starting material | Ref. |
|---|---|---|---|---|---|
| **etched meso-$TiO_2$ (ME20h)** | **150 W Xe lamp, air mass 1.5G filter, 50 mg photocatalyst, 150 mL 10 vol% methanol aqueous solution** | **0.1 wt% Pt** | **106.7** | **102%** | **This work** |
| **short conversion time of meso-$TiO_2$ (MC0.5h)** | **150 W Xe lamp, air mass 1.5G filter, 50 mg photocatalyst, 150 mL 10 vol% methanol aqueous solution** | **0.1 wt% Pt** | **71.5** | **35%** | **This work** |
| $SrTiO_3/TiO_2$ | 300 W Xe lamp, no filter, 50 mg photocatalyst, 100 mL 10 vol% methanol aqueous solution | 1 wt% Pt | 650.3 | cannot be determined | [1] |
| $SrTiO_3/TiO_2$ | 300 W Xe lamp, 200-2500 nm, 100 mg photocatalyst, 100 mL 6 M methanol aqueous solution | no co-catalyst | 90.3 (averaged from 8 h experiment) | 138% | [2] |
| $SrTiO_3/TiO_2$ | 300 W Xe lamp, no filter, 100 mg photocatalyst, 100 mL 20 vol% methanol aqueous solution | 0.3 wt% Pt | 664 | cannot be determined precisely | [3] |
| $SrTiO_3/TiO_2$ | 300 W Xe lamp, no filter, 10 mg photocatalyst, 40 mL 10 vol% methanol aqueous solution | 5 wt% $HAuCl_4 \cdot H_2O$ | 3.3 | 924% | [4] |
| $SrTiO_3/TiO_2$ | 250 W Hg lamp, no filter, 10 mg photocatalyst, 35 mL 25 vol% methanol aqueous solution | 3.5 wt% Pt | 1112.6 | 152% | [5] |
| $SrTiO_3/TiO_2$ | 300 W Xe lamp, no filter, 50 mg photocatalyst, 99 mL 20 vol% triethanolamine aqueous solution | 1 wt% Pt | 18.7 | 154% | [6] |
| $SrTiO_3/TiO_2$ | 400 W Hg lamp, no filter, 0.5 g/L photocatalyst methanol aqueous solution | no co-catalyst | approx. 750 | cannot be determined precisely | [7] |

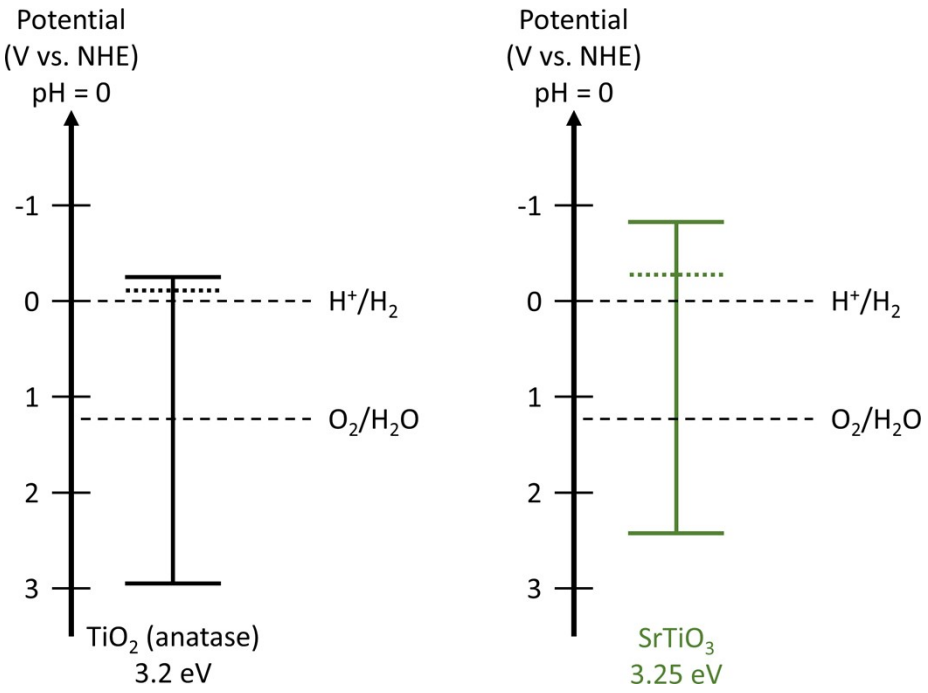


Figure S35: Band edge positions and fermi levels (dotted line) of $TiO_2$ (anatase) and $SrTiO_3$ relative to the normal hydrogen electrode (NHE). Values are based on experimental data from references [8–12].

## Overall water splitting (OWS)

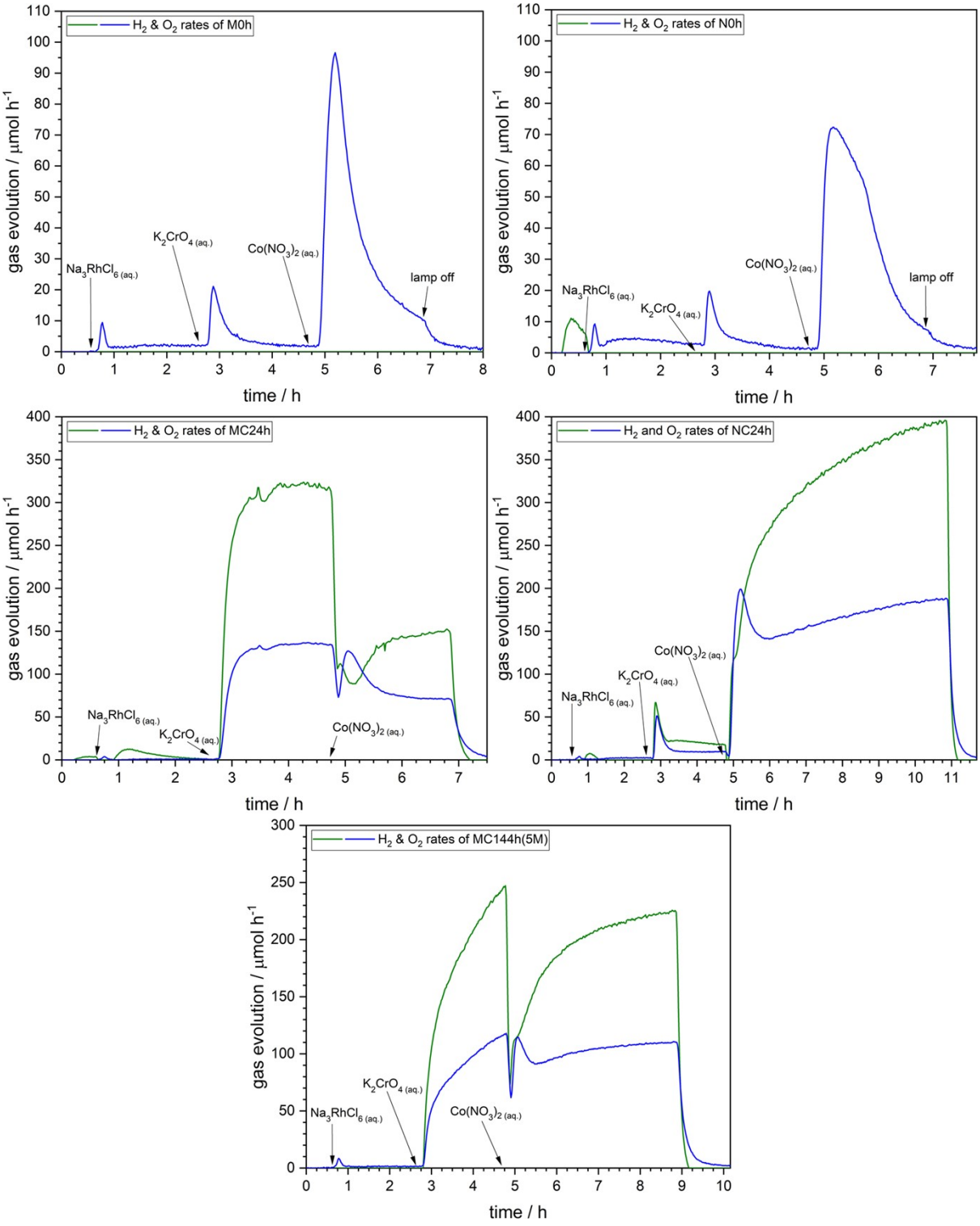


Figure S36: Photocatalytic OWS of the starting materials M0h and N0h and the converted samples MC24h, NC24h, and MC144h(5M).

Post photocatalysis (OWS):

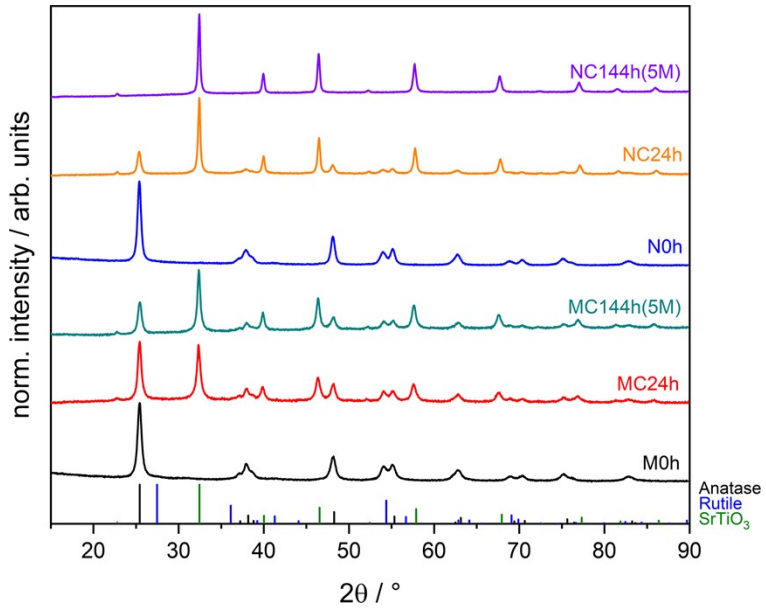


Figure S37: XRD patterns after photocatalytic OWS experiments.

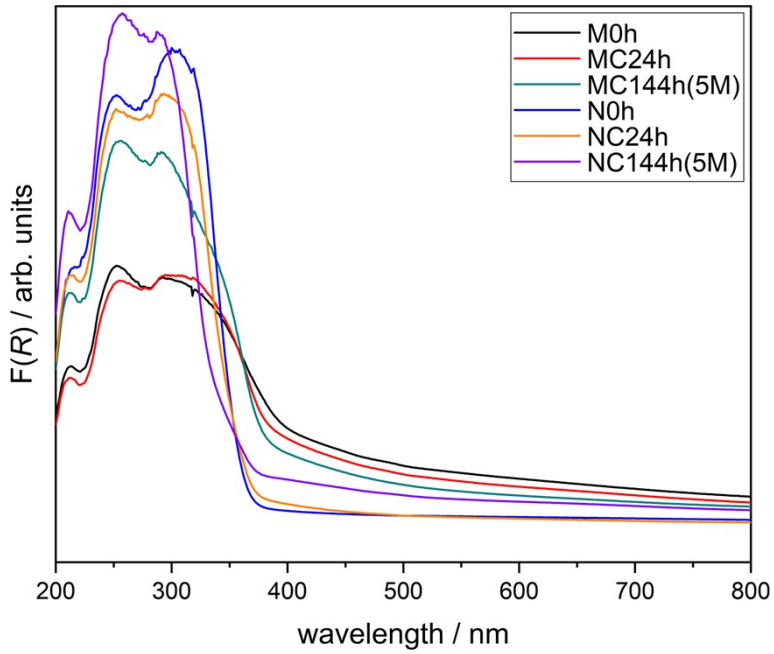


Figure S38: Kubelka-Munk plots after photocatalytic OWS experiments.

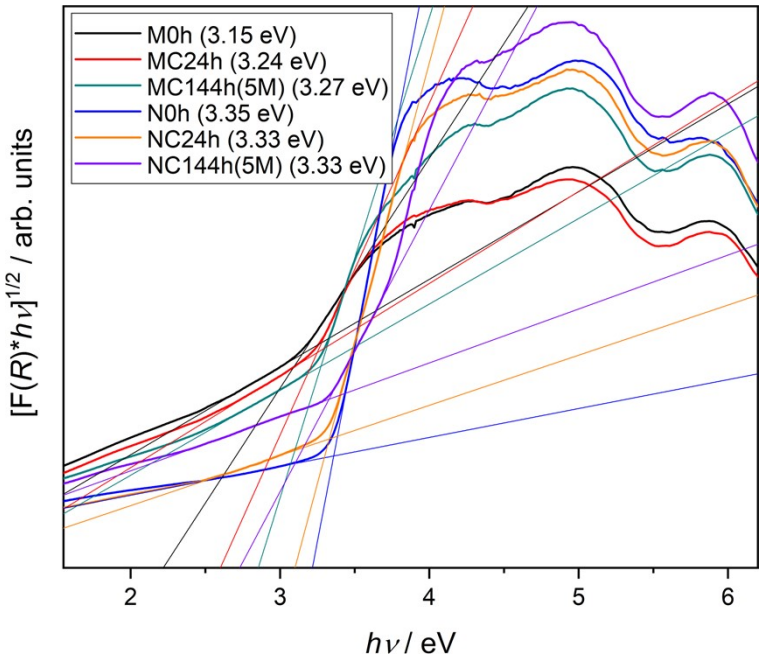


Figure S39: Tauc plots after photocatalytic OWS experiments. High amounts of co-catalyst lead to steeper background fits.

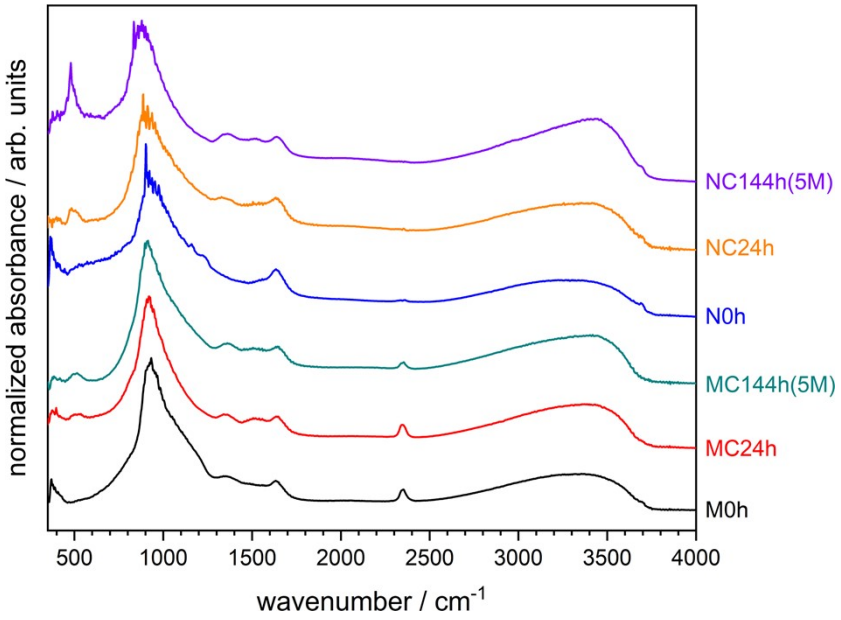


Figure S40: DRIFT spectra after photocatalytic OWS experiments.

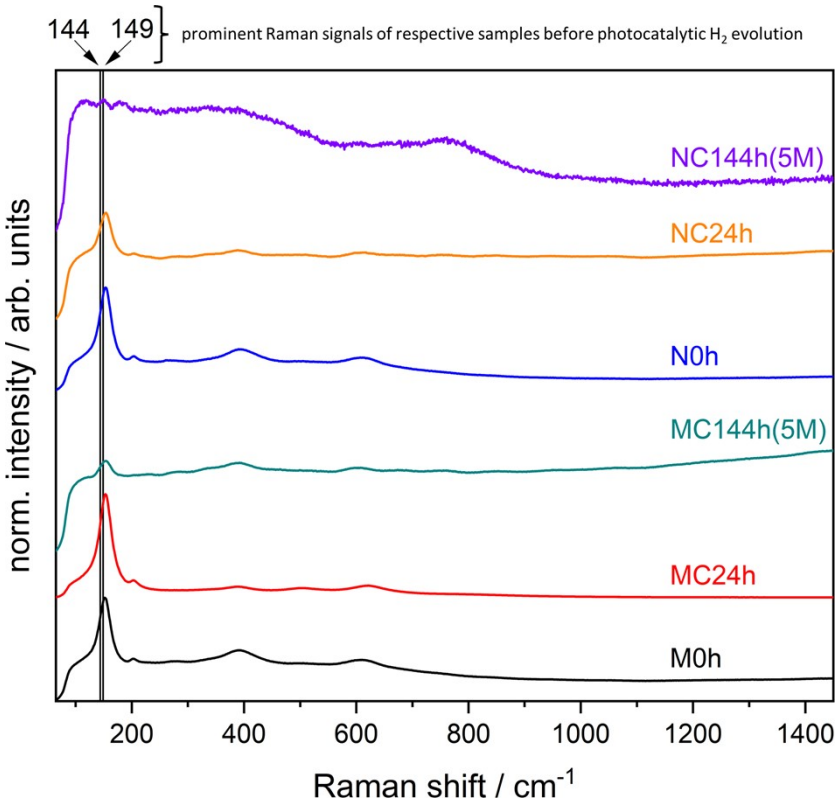


Figure S41: Raman spectra after photocatalytic OWS experiments. Photodeposited co-catalysts lead to broad intensities, which shift signals of the samples compared to spectra before photocatalysis.

References


1 Y. He, L. Zhang, Y. Wei, X. Zhang, Z. Wang and R. Yu, *Small Methods*, 2022, **6**, 2101567.

2 M. N. Ha, F. Zhu, Z. Liu, L. Wang, L. Liu, G. Lu and Z. Zhao, *RSC Adv.*, 2016, **6**, 21111–21118.

3 Z. Zhuo, X. Wang, C. Shen, M. Cai, Y. Jiang, Z. Xue, Z. Fu, Q. Wang, Y. Wei and S. Sun, *Chem. Eur. J.*, 2023, **29**, e202203450.

4 C. Hu, C. Tai, W. Zhang, Q. Lu, M. Wei, C. Si, E. Guo and Y. Pang, *J. Alloys Compd.*, 2023, **930**, 167449.

5 L. Yang, Z. Chen, J. Zhang and C. A. Wang, *Front. Mater. Sci.*, 2019, **13**, 342–351.

6 Y. Yang, Y. Zhang, T. Wang, Y. Ma, S. Xing, J. Yan, J. Ran and X. Li, *Catal. Letters*, 2024, **154**, 2537–2550.

7 H. Bai, J. Juay, Z. Liu, X. Song, S. S. Lee and D. D. Sun, *Appl. Catal. B Environ.*, 2012, **125**, 367–374.

8 J. ichi Fujisawa, T. Eda and M. Hanaya, *Chem. Phys. Lett.*, 2017, **685**, 23–26.

9 V. J. Babu, S. Vempati, T. Uyar and S. Ramakrishna, *Phys. Chem. Chem. Phys.*, 2015, **17**, 2960–2986.

10 Y. W. Chung and W. B. Weissbard, *Phys. Rev. B*, 1979, **20**, 3456–3461.

11 W. Sun, S. Meng, S. Zhang, X. Zheng, X. Ye, X. Fu and S. Chen, *J. Phys. Chem. C*, 2018, **122**, 15409–15420.

12 V. Pfeifer, P. Erhart, S. Li, K. Rachut, J. Morasch, J. Brötz, P. Reckers, T. Mayer, S. Rühle, A. Zaban, I. Mora Seró, J. Bisquert, W. Jaegermann and A. Klein, *J. Phys. Chem. Lett.*, 2013, **4**, 4182–4187.